



Early Results from GLASS-JWST. XXIV. The Mass–Metallicity Relation in Lensed Field Galaxies at Cosmic Noon with NIRISS*

Xianlong He^{1,2} , Xin Wang^{1,3,4} , Tucker Jones⁵ , Tommaso Treu⁶ , K. Glazebrook⁷ , Matthew A. Malkan⁶ , Benedetta Vulcani⁸ , Benjamin Metha^{6,9,10} , Maruša Bradac^{5,11} , Gabriel Brammer^{12,13} , Guido Roberts-Borsani⁶ , Victoria Strait^{12,13} , Andrea Bonchi^{14,15} , Marco Castellano¹⁵ , Adriano Fontana¹⁵ , Charlotte Mason^{12,13} , Emiliano Merlin¹⁵ , Takahiro Morishita¹⁶ , Diego Paris¹⁵ , Paola Santini¹⁵ , Michele Trenti^{9,10} , Kristan Boyett^{9,10} , and K. Grasha^{10,17,18,19}

¹ School of Astronomy and Space Science, University of Chinese Academy of Sciences (UCAS), Beijing 100049, People's Republic of China; xwang@ucas.ac.cn

² School of Physics and Technology, Wuhan University (WHU), Wuhan 430072, People's Republic of China

³ National Astronomical Observatories, Chinese Academy of Sciences, Beijing 100101, People's Republic of China

⁴ Institute for Frontiers in Astronomy and Astrophysics, Beijing Normal University, Beijing 102206, People's Republic of China

⁵ Department of Physics and Astronomy, University of California, Davis, 1 Shields Avenue, Davis, CA 95616, USA

⁶ Department of Physics and Astronomy, University of California, Los Angeles, 430 Portola Plaza, Los Angeles, CA 90095, USA

⁷ Centre for Astrophysics and Supercomputing, Swinburne University of Technology, PO Box 218, Hawthorn, VIC 3122, Australia

⁸ INAF Osservatorio Astronomico di Padova, vicolo dell'Osservatorio 5, I-35122 Padova, Italy

⁹ School of Physics, University of Melbourne, Parkville, VIC 3010, Australia

¹⁰ ARC Centre of Excellence for All Sky Astrophysics in 3 Dimensions (ASTRO 3D), Australia

¹¹ University of Ljubljana, Department of Mathematics and Physics, Jadranska ulica 19, SI-1000 Ljubljana, Slovenia

¹² Cosmic Dawn Center (DAWN), Denmark

¹³ Niels Bohr Institute, University of Copenhagen, Jagtvej 128, DK-2200 Copenhagen N, Denmark

¹⁴ Space Science Data Center, Italian Space Agency, via del Politecnico, I-00133 Roma, Italy

¹⁵ INAF Osservatorio Astronomico di Roma, Via Frascati 33, I-00078 Monteporzio Catone, Rome, Italy

¹⁶ IPAC, California Institute of Technology, MC 314-6, 1200 E. California Boulevard, Pasadena, CA 91125, USA

¹⁷ Research School of Astronomy and Astrophysics, Australian National University, Canberra, ACT 2611, Australia

¹⁸ Visiting Fellow, Harvard-Smithsonian Center for Astrophysics, 60 Garden Street, Cambridge, MA 02138, USA

Received 2023 September 14; revised 2023 November 21; accepted 2023 November 30; published 2024 January 8

Abstract

We present a measurement of the mass–metallicity relation (MZR) at Cosmic Noon, using the JWST near-infrared wide-field slitless spectroscopy obtained by the GLASS-JWST Early Release Science program. By combining the power of JWST and the lensing magnification by the foreground cluster A2744, we extend the measurements of the MZR to the dwarf mass regime at high redshifts. A sample of 50 galaxies with several emission lines is identified across two wide redshift ranges of $z = 1.8\text{--}2.3$ and $2.6\text{--}3.4$ in the stellar mass range of $\log(M_*/M_\odot) \in [6.9, 10.0]$. The observed slope of MZR is 0.223 ± 0.017 and 0.294 ± 0.010 at these two redshift ranges, respectively, consistent with the slopes measured in field galaxies with higher masses. In addition, we assess the impact of the morphological broadening on emission line measurement by comparing two methods of using 2D forward modeling and line profile fitting to 1D extracted spectra. We show that ignoring the morphological broadening effect when deriving line fluxes from grism spectra results in a systematic reduction of flux by $\sim 30\%$ on average. This discrepancy appears to affect all the lines and thus does not lead to significant changes in flux ratio and metallicity measurements. This assessment of the morphological broadening effect using JWST data presents, for the first time, an important guideline for future work deriving galaxy line fluxes from wide-field slitless spectroscopy, such as Euclid, Roman, and the Chinese Space Station Telescope.

Unified Astronomy Thesaurus concepts: Strong gravitational lensing (1643); Galaxy photometry (611); Galaxy spectroscopy (2171); Dwarf galaxies (416); High-redshift galaxies (734); Abell clusters (9); Metallicity (1031)

1. Introduction

Nearly all elements heavier than helium (referred to as metals in astronomy) are synthesized by stellar nuclear reactions, making them a good tracer of star formation activity across cosmic time. Star formation rate (SFR) and metal enrichment peak at the “Cosmic Noon” epoch $z \sim 2$ (Madau & Dickinson 2014,

Figure 9), confirmed by a census of deep surveys with Hubble Space Telescope (HST), the Sloan Digital Sky Survey (SDSS), and other facilities. Metals are thought to be expelled into the interstellar/intergalactic medium (ISM/IGM) by stellar explosions such as supernovae and stellar winds. The cumulative history of the baryonic mass assembly, e.g., star formation, gas accretion, mergers, feedback, and galactic winds, altogether governs the total amount of metals remaining in gas (Finlator & Davé 2008; Davé et al. 2012; Lilly et al. 2013; Dekel & Mandelker 2014; Peng & Maiolino 2014). Therefore, the elemental abundances provide a crucial diagnostic of the past history of star formation and complex gas movements driven by galactic feedback and tidal interactions (Lilly et al. 2013; Maiolino & Mannucci 2019). Since detailed abundances are not directly measurable at extragalactic distances, the relative oxygen

* Based on observations acquired by JWST under the ERS program ID 1324 (PI: T. Treu).

¹⁹ ARC DECRA Fellow.



abundance (number density) compared to hydrogen in ionized gaseous nebulae (reported as $12 + \log(\text{O}/\text{H})$), is often chosen as the observational proxy of *metallicity* for simplicity.

Several scaling relations have been established, characterizing the tight correlations between various physical properties of star-forming galaxies, e.g., stellar mass (M_*), metallicity Z , SFR, luminosity, size, and morphology (see Kewley et al. 2019; Maiolino & Mannucci 2019 for recent reviews). Metallicity abundance evolution was found to exhibit a strong correlation with mass during galaxy evolution history (Davé et al. 2011; Lu et al. 2015b). The mass–metallicity relation (MZR), has been quantitatively established in the past two decades in both the local (Tremonti et al. 2004; Zahid et al. 2012; Andrews & Martini 2013, mainly from SDSS), and the distant universe out to $z \sim 3$ (Erb et al. 2006; Maiolino et al. 2008; Zahid et al. 2011; Henry et al. 2013b; Sanders et al. 2015; Guo et al. 2016; Henry et al. 2021; Sanders et al. 2021; Pharo et al. 2023). Recently, the launch of JWST has enabled the measurement of the MZR out to $z \sim 8$ (e.g., Arellano-Córdova et al. 2022; Schaerer et al. 2022; Curti et al. 2023b, 2023a; Matthee et al. 2023; Nakajima et al. 2023; Rhoads et al. 2023; Sanders et al. 2023; Trump et al. 2023). The slope of the MZR is sensitive to the properties of outflows (e.g., mass loading factor, gas outflow velocity), which are a crucial ingredient to galaxy evolution models (see Davé et al. 2012; Lu et al. 2015a; Henry et al. 2021). The MZR slope has also been used to reveal trends in how the star formation efficiency and galaxy gas mass fraction depend on stellar mass (Baldry et al. 2008; Zahid et al. 2014). Mannucci et al. (2010) first suggested a so-called fundamental metallicity relation (FMR), which aims to explain the scatter and redshift evolution of the MZR by introducing the SFR as an additional variable, creating a three-parameter scaling relation. The FMR has a small intrinsic scatter of ~ 0.05 dex in metallicity, making it possible to trace the metal production rates in stellar within cosmological time (Finlator & Davé 2008). Moreover, spatially resolved chemical information encoded by the metallicity radial gradients (Jones et al. 2015b; Wang et al. 2017, 2019, 2020; Franchetto et al. 2021; Wang et al. 2022b) is a sensitive probe of baryonic assembly and the complex gas flows driven by both galactic feedback and tidal interactions.

The Near-infrared Imager and Slitless Spectrograph (NIRISS; Willott et al. 2022) on board JWST now enables a tremendous leap forward with its superior sensitivity, angular resolution, and longer wavelength coverage compared to HST/WFC3. This allows metallicity measurements with better precision in galaxies with lower stellar mass at the Cosmic Noon epoch $1 < z < 3$. Similar measurements have been done using data from NIRSpec gratings (e.g., Curti et al. 2023a; Shapley et al. 2023), NIRSpec prism (Langeroodi et al. 2023), and NIRCам WFSS (Matthee et al. 2023), and NIRISS (Li et al. 2023). This paper takes advantage of the deep NIRISS spectroscopy acquired by the Early Release Science (ERS) program GLASS-JWST (ID ERS-1324²⁰; Treu et al. 2022) in the field of the galaxy cluster A2744. By exploiting the gravitational lensing magnification produced by the foreground A2744 cluster, we are able to extend the measurement of the MZR down to 10^7 solar mass M_\odot .

In this paper, we present a measurement of the MZR using the NIRISS and NIRCам data from a sample of 50 lensed field

galaxies in a low mass range at $z \sim 2-3$. In Section 2, we describe the data acquisition and galaxy sample analyzed in this work. In Section 3, we demonstrate our method to extract metallicity and stellar mass for both individual galaxies and their stacked spectrum. The main goal of this work is to present our MZR measurements. We discuss the results in Section 4 and summarize the main conclusions in Section 5. The AB magnitude system, the standard concordance cosmology ($\Omega_m = 0.3$, $\Omega_\Lambda = 0.7$, $H_0 = 70 \text{ km s}^{-1} \text{ Mpc}^{-1}$), and the Chabrier (2003) initial mass function are adopted. The metallicity lines are denoted in the following manner, if presented without wavelength: $\text{O II } \lambda\lambda 3727, 3730 := \text{O II}$; $\text{Ne III } \lambda 3869 := \text{Ne III}$; $\text{H } \gamma \lambda 4342 := \text{H } \gamma$; $\text{H } \beta \lambda 4863 := \text{H } \beta$; $\text{O III } \lambda 5008 := \text{O III}$; $\text{H } \alpha \lambda 6564 := \text{H } \alpha$; and $\text{S II } \lambda\lambda 6716, 6731 := \text{S II}$.

2. Observation Data

We use the joint JWST NIRISS and NIRCам data targeting the A2744 lensing field cluster. The NIRISS data are used to estimate the metallicity through modeling of emission line flux ratios, while the NIRCам data are used to calculate the stellar mass through spectral energy distribution (SED) Fitting.

The spectroscopy data from JWST/NIRISS of GLASS-ERS (program DD-ERS-1324, PI: T. Treu), with the observing strategy described by Treu et al. (2022), is reduced in Paper I (Roberts-Borsani et al. 2022). Briefly, the core of the A2744 cluster ($130'' \times 130''$) was observed for ~ 18.1 hr with NIRISS wide-field slitless spectroscopy and direct imaging for ~ 2.36 hr in three filters (F115W, F150W, and F200W)²¹ on 2022 June 28–29 and 2023 July 7. The total exposure times for the majority of sources in each of these three bands amount to 5.4, 5.7, and 2.9 hr (as detailed in Figure 1). This provides low-resolution $R := \lambda/\Delta\lambda \sim 150$ spectra of all objects in the field of view with continuous wavelength coverage from $\lambda \in [1.0, 2.2] \mu\text{m}$. This includes the strong rest-frame optical emission lines [O II], [Ne III], H γ , H β , [O III] at $z \in [1.8, 3.4]$, and H α , [S II] at $z \in [1.8, 2.3]$.²² Spectra are taken at two orthogonal dispersion angles (using the GR150C and GR150R grism elements), which helps to minimize the effects of contamination by overlapping spectral traces.

The photometric data of the A2744 cluster we used are the publicly released NIRCам images (Paris et al. 2023), coming from three programs: GLASS-JWST (PI: Treu), UNCOVER (PIs: Bezanson and Labbé), and DDT-2756 (PI: Chen). It is an F444W-detected multiband catalog, including all NIRCам and available HST data. All reduced images in eight JWST/NIRCам bands (F090W, F115W, F150W, F200W, F277W, F356W, F410M, and F444W), four HST/ACS-WFC bands (F435W, F606W, F775W, and F814W), and four HST/WFC3-IR bands (F105W, F125W, F140W, and F160W)²³ are used if available. This photometric data, with an observed-frame wavelength coverage of $0.4-5 \mu\text{m}$ at redshift $z \in [1.8, 3.4]$, enable very good stellar mass estimates by sampling the full rest-UV to near-IR SEDs. We also use the half-light radius r_{50} of this catalog in Section 4.2. The half-light radius r_{50} is

²¹ See the official documentation for more information: <https://jwst-docs.stsci.edu/jwst-near-infrared-imager-and-slitless-spectrograph/niriss-observing-modes/niriss-wide-field-slitless-spectroscopy>.

²² Li et al. (2023) have developed an interactive website to visualize the emission lines covered by each filter at different redshifts: <https://preview.lmytime.com/jwstfilter>.

²³ See the repository of the Spanish Virtual Observatory for more Filter information: <http://svo2.cab.inta-csic.es/theory/fps/>.

²⁰ <https://www.stsci.edu/jwst/science-execution/approved-programs/dd-ers/program-1324>

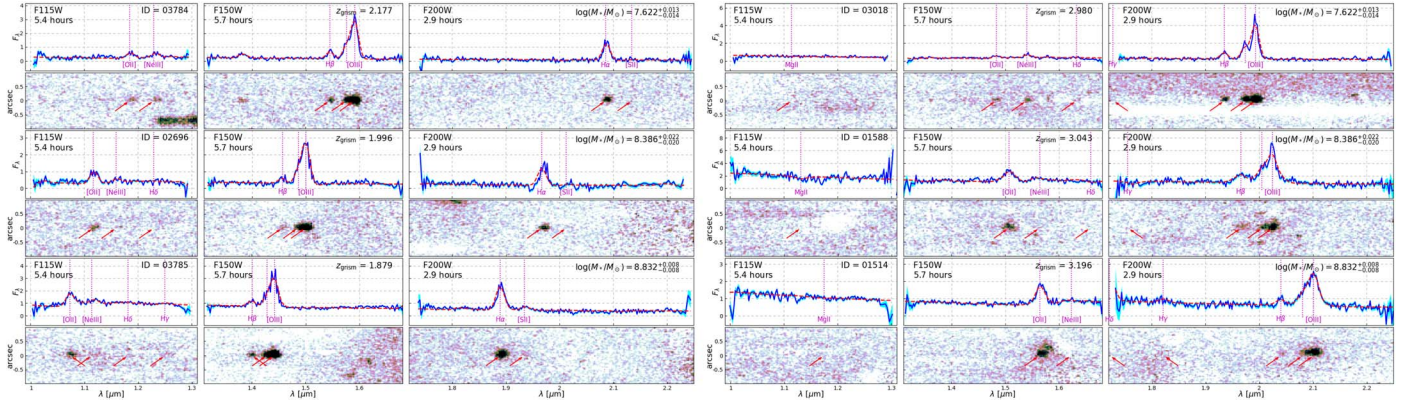


Figure 1. 1D/2D spectra of six galaxies in our sample. Left: three examples at $z = 1.8\text{--}2.3$. The forward-modeled spectra, optimally extracted 1D observed flux F_λ (in units of $[10^{-19} \text{ erg/s/cm}^2/\text{\AA}]$), and its 1σ uncertainty, are represented by the red and blue solid lines and the cyan shaded bands, respectively. The 2D grism spectra covered in three filters (F115W, F150W, and F200W) are continuum-subtracted. Right: same as the left panel, but at $z = 2.6\text{--}3.4$.

computed by SEXTRACTOR in the F444W band in units of pixel (the effective radius FLUX_RADIUS in SEXTRACTOR).

3. Measurements

In this section, we present the measurements of the physical properties derived from spectroscopy and photometry, with the result of 50 individual galaxies shown in Table A1.

Quantities (e.g., the stellar mass M_* and SFR) that are derived from a single flux must be corrected for the modest gravitational lensing magnification by the foreground A2744 cluster. But properties that are derived from flux ratio (e.g., metallicity Z) or other observed quantities, are independent of lensing magnification. We adopt our latest high-precision, JWST-based lensing model (Bergamini et al. 2023a, 2023b) to estimate the lensing magnification μ . We do not consider the uncertainty of μ because the relative error is only $\sim 2.3\%$. The median estimate of μ is consistent but more precise with the calculation derived from the public Hubble Frontier Fields (HFF) lensing tool²⁴ (Lotz et al. 2017) using the Sharon & Johnson version (Johnson et al. 2014) and the CATS version (Jauzac et al. 2015) computed by LENSTOOL software²⁵ (Petri 2016).

3.1. Grism Redshift and Emission Line Flux

We utilize the Grism Redshift and Line Analysis software GRIZLI (Brammer 2023) to reduce NIRISS data using the standard JWST pipeline (version 1.11.1) and the latest reference file (under the JWST_1100.PMAP context). The detailed procedures are largely described in Roberts-Borsani et al. (2022). Briefly, GRIZLI analyzes the paired direct imaging and grism exposures through forward modeling and yields contamination-subtracted 1D and 2D grism spectra, along with the best-fit spectroscopic redshifts.

For each source, the 1D spectrum is constructed using a linear superposition of a spectra from a library consisting of four sets of empirical continuum spectra covering a range of stellar population ages (Brammer et al. 2008; Erb et al. 2010; Conroy & van Dokkum 2012; Muzzini et al. 2013) and Gaussian-shaped nebular emission lines at the observed wavelengths given by the source redshift. The intrinsic 1D spectrum and the spatial distribution of flux measured in the

paired direct image are utilized to generate a 2D model spectrum based on the grism sensitivity and dispersion function, similar to the “fluxcube” model produced by the aXe software (Walsh et al. 2009). This 2D forward-modeled spectrum is then compared to the observation by GRIZLI and a global χ^2 calculation is performed to determine the best-fit superposition coefficients for both the continuum templates and Gaussian amplitudes, the latter of which correspond to the best-fit emission line fluxes. In this way, our 2D forward-modeling practice not only determines the source redshift, but also measures the emission line fluxes, taking into account the morphological broadening effect. We refer the interested readers to Appendix A of Wang et al. (2019), for the full descriptions of the redshift fitting procedure.

We obtain a parent sample of 4756 sources with F150W apparent magnitudes between [18, 32] ABmag (the 5σ depth is 28.7 according to Treu et al. 2022), on which our GRIZLI analyses result in meaningful redshift constraints. Several goodness-of-fit criteria are implemented to ensure the reliability of our redshift fit: a reduced chi-square close to 1 ($\chi^2 < 2.2$), a sharply peaked posterior of the redshift $(\Delta z)_{\text{posterior}}/(1 + z_{\text{peak}}) < 0.002$, high evidence of Bayesian information criterion compared to polynomials ($\text{BIC} > 100$). As a result, there are 348 sources in the redshift range $z \in [0.05, 10]$, with secure grism redshift measurements according to the above joint selection criteria. A total of 86 sources with secure grism redshifts are at redshifts $z \in [1.8, 2.3] \cup [2.6, 3.4]$, ensuring that the slitless spectra cover several emission lines: [O II], [Ne III], H δ , H γ , H β , and [O III] (also H α , [S II] for the former zone), with high sensitivity for our three NIRISS filters (F115W, F150W, and F200W). However, 6/86 sources of our NIRISS spectroscopy catalog do not match entries in the NIRCcam photometric catalog (Paris et al. 2023) within $0''.7$ ($5 \times \text{PSF}$).

The fluxes of the intrinsic nebular emission lines ([O II], [Ne III], H δ , H γ , H β , [O III], H α , and [S II], the same as in Henry et al. 2021) are 2D forward modeled by GRIZLI as output. There are 57 sources with H β detection, to ensure the reliable measurement of SFR. No other emission line criteria (e.g., S/N [O III]) are used for selection, to avoid potential metallicity bias. Then we visually inspect the 1D spectra of each galaxy individually, excluding seven of those that are heavily contaminated. The 50 galaxies showing prominent nebular emission features, with zero possible active galactic nucleus (AGN) exclusions in Section 3.4, will make up the

²⁴ <https://archive.stsci.edu/prepds/frontier/lensmodels/>

²⁵ <https://lenstools.readthedocs.io/en/latest/>

Table 1
Coefficients for the Emission Line Flux Ratio Diagnostics Used in This Work

Diagnostic R and Notation	c_0	c_1	c_2	c_3	c_4	c_5	σ^{cal}	ref
$O_3 := [\text{O III}]/\text{H}\beta$	43.9836	-21.6211	3.4277	-0.1747	0.05	(Bian et al. 2018, B18)
$O_2 := [\text{O II}]/\text{H}\beta$	78.9068	-45.2533	7.4311	-0.3758	0.05	
$\text{H}\alpha/\text{H}\beta$	0.45637	0.00	Balmer decrement
$\text{H}\gamma/\text{H}\beta$	-0.32790	0.00	
$\text{Ne}_3\text{O}_3 := [\text{Ne III}]/[\text{O III}]$	-1.11420	0.04	Jones et al. (2015a)
$S_2 := [\text{S II}]/\text{H}\alpha$	-0.54571	0.45730	-0.82269	-0.02839	0.59396	0.34258	best	Jones et al. (2015a) ^b
	-0.43974	0.34034	-0.62850	-0.07077	0.47147	0.31767	upper	
	-0.65464	0.58976	-1.06047	0.01979	0.75382	0.37766	lower	

Notes.

^a We note that the $[\text{O III}]/\text{H}\beta$ calibration reported in Bian et al. (2018) in fact refers to the flux ratio between $[\text{O III}]$ 4960,5008 and $\text{H}\beta$, i.e., a factor of (2.98/3.98) is needed (following Storey & Zeippen 2000) when we use the doublets let to calibrate pure $[\text{O III}]$ 5008.

^b The line flux ratio $R_{[\text{S II}]}$ is calibrated by polynomial with coefficients given by the “best” row, and the uncertainty $\sigma_{[\text{S II}]}$ is given by the “upper” and “lower” rows, where the metallicity x is relative to solar $x := 12 + \log(\text{O}/\text{H}) - 8.69$.

final sample presented in Table A1. A “textbook case” of our samples (ID: 05184 in Table A1) has been carefully studied through spatial mapping in our recent work (Wang et al. 2022a). We show as an example 1D/2D spectra for six galaxies in our sample in Figure 1, annotated with their exposure times, best-fit grism redshifts, and stellar masses (which will be discussed in Section 3.3).

Since the 1D grism spectra are extracted by GRIZLI simultaneously, it allows us to directly fit it using several 1D Gaussian profiles to obtain line fluxes and errors, as detailed in Section 3.5. But we still use the previous 2D flux other than 1D as our default result for subsequent calculations. The comparison of the line flux measurements between this 1D line profile fitting and the 2D GRIZLI forward-modeling procedure, is discussed in Section 4.2.

3.2. Gas-phase Metallicity and Star Formation Rate

We use these observed line fluxes (f_i^o , σ_i^o) to simultaneously estimate three parameters: jointly metallicity, nebular dust extinction, and dereddened $\text{H}\beta$ line flux ($12 + \log(\text{O}/\text{H})$, A_v , $f_{\text{H}\beta}$). We follow the previous series of work (Jones et al. 2015b; Wang et al. 2017, 2019, 2020, 2022b) by constructing a Bayesian inference method that uses multiple calibration relations to jointly constrain metallicity $12 + \log(\text{O}/\text{H})$ and (A_v , $f_{\text{H}\beta}$) simultaneously. Our method is more reliable than the conventional way of turning line flux ratios into metallicities, since it takes into account the intrinsic scatter in strong line O/H calibrations (σ_{R_i} in Equation (1)). And it combines multiple line flux measurements and properly marginalizes over the dust extinction correction. It also emphasizes bright lines (e.g., $[\text{O II}]$, $[\text{O III}]$) with high signal-to-noise ratios (S/Ns) and marginalizes faint lines (e.g., $\text{H}\beta$) or even nondetection lines with low S/Ns quantitatively, (i.e., by assigning weights to each line according to its S/N in the likelihood function).

The Markov Chain Monte Carlo (MCMC) sampler EMCEE software (Foreman-Mackey et al. 2013) is employed to sample the likelihood profile $\mathcal{L} \propto \exp(-\chi^2/2)$ with

$$\chi^2 := \sum_i^{\text{EL}} \frac{(f_i - R_i \cdot f_{\text{H}\beta})^2}{(\sigma_i^o)^2 + (\sigma_{R_i})^2 \cdot f_{\text{H}\beta}^2}, \quad R_i := \frac{f_i}{f_{\text{H}\beta}}. \quad (1)$$

Here the summation i includes all emission lines, with their intrinsic scatters $\sigma_{R_i} := \sigma_i^{\text{cal}} \cdot R_i \cdot \ln 10$. The inherent flux and uncertainty (f_i , σ_i) for each line are corrected from observation (f_i^o , σ_i^o) for dust attenuation by parameter A_v using the Calzetti et al. (2000) extinction law. R_i refers to the line flux ratio, which is empirically calibrated by a polynomial as a function of metallicity: $\log R = \sum_{j=0}^n c_j \cdot (x)^j$, $x := 12 + \log(\text{O}/\text{H})$, where $(x)^j$ means j th power of x , with the coefficients summarized in Table 1. For flux ratio calibrations that do not use $\text{H}\beta$ as the denominator (e.g., $[\text{Ne III}]/[\text{O III}]$), the terms $f_{\text{H}\beta}$ in Equation (1) need to be replaced by the corresponding lines (e.g., $f_{[\text{O III}]}$). And one more term of uncertainty (e.g., $\sigma_{O_3}^2 \cdot R_{\text{Ne}_3\text{O}_3}^2$) needs to be added to the denominator of χ^2 .

A wide range of strong line calibrations between line flux ratio and metallicity has been established (see Appendix C in Wang et al. 2019 for a summary; also see Kewley et al. 2019; Maiolino & Mannucci 2019 for recent reviews). Different choices can result in offsets as high as 0.7 dex (see, e.g., Kewley & Ellison 2008). In this work, we adopt mainly the diagnostics group “ $\text{O}_3\text{--O}_2$ ” of calibrations prescribed by Bian et al. (2018, hereafter B18), for comparison with Sanders et al. (2021) and Wang et al. (2022b). The purely empirical calibrations in Bian et al. (2018, B18) are based on a sample of local analogs of high- z galaxies according to the location on the Baldwin, Phillips & Terlevich (BPT) diagram (Baldwin et al. 1981), with the notations and coefficients summarized in Table 1.

These calibrations are recommended for the metallicity range of $7.8 < 12 + \log(\text{O}/\text{H})$, which is appropriate for our sample that does not reach metallicities as low as those found at higher redshift (Curti et al. 2023b; Heintz et al. 2023). As a sanity check, we computed metallicities using the calibrations from Sanders et al. (2023), and indeed we do not find galaxies with metallicities significantly lower than 7.8. In order to make complete use of emission lines of spectra, we also collect Ne_3O_3 , S_2 diagnostics at the same time, even though the corresponding line fluxes are not so strong for our sample. We have tested that if they are removed, they do not significantly affect the metallicity estimation, which is dominated by the first two diagnostics O_3 , O_2 in B18 and two Balmer decrements. We adopt the intrinsic Balmer decrement flux ratios assuming case

B recombination with $T_e \sim 10,000$ K. We neglect the line-blending effect, since they are likely small in most cases (see Figure 4 and Appendix C in Henry et al. 2021 for more information). This Bayesian method is used to derive properties ($12 + \log(\text{O}/\text{H})$, A_v , $f_{\text{H}\beta}$) of galaxies both from our individual spectra sample here and from the stacked spectra presented in Section 3.5.

From the dereddened $\text{H}\beta$ flux $f_{\text{H}\beta}$, we estimate the instantaneous SFR of our sample galaxies, based on Balmer line luminosities. This approach provides a valuable proxy of the ongoing star formation on a timescale of ~ 10 Myr, highly relevant for galaxies displaying strong nebular emission lines. Assuming the Kennicutt (1998) calibration and the Balmer decrement ratio of $\text{H}\alpha/\text{H}\beta = 2.86$ from the case B recombination for typical H II regions, we calculate

$$\text{SFR} = 4.65 \times 10^{-42} \frac{L(\text{H}\beta)}{[\text{erg s}^{-1}]} \times 2.86 [M_\odot \text{ yr}^{-1}], \quad (2)$$

suitable for the Chabrier (2003) initial mass function. The total luminosity $L(\text{H}\beta) = 4\pi D_L^2(z) \cdot f_{\text{H}\beta}$ is corrected for lensing magnification according to Bergamini et al. (2023a). The corrected SFR values are given in Table A1.

3.3. Stellar Mass and Lensing Magnification

In this section, we fit broadband photometry to obtain stellar mass M_* of target galaxies through SED fitting. We directly use the combined photometric catalog released by the GLASS-JWST team (Paris et al. 2023). The photometric fluxes measured within $2 \times \text{PSF FWHM}$ apertures of all 16 bands are included if available. We match 2983/4756 galaxies of our NIRISS spectroscopy catalog in Section 3.1 to the 24,389 galaxies of the NIRCам photometric catalog with on-sky distances (d2d) lower than $0''.7$ ($5 \times \text{FWHM}$ in the F444W band, conservatively). As done in Section 3.1, the final selected sample of 50 galaxies yields accurate d2d match ($< 0''.14$, around the angular resolution of JWST/NIRISS), and visually crossmatching with the NIRCам image further validates our sources.

To estimate the stellar masses M_* of our sample galaxies, we use the BAGPIPES software (Carnall et al. 2018) to fit the BC03 (Bruzual & Charlot 2003) models of SEDs to the photometric measurements derived above. We assume the Chabrier (2003) initial mass function, a metallicity range of $Z/Z_\odot \in (0, 2.5)$, and the Calzetti et al. (2000) extinction law with A_v in the range of $(0, 3)$. We use the double power-law (DPL) model rather than the simple exponentially declining form to capture the complex star formation history (SFH) of our galaxies at Cosmic Noon (rather than local Universe), following Carnall et al. (2019). The nebular emission component is also added into the SED during the fit, since our galaxies are exclusively strong line emitters by selection. The redshifts of our galaxies are fixed to their best-fit grism values, with a conservative uncertainty of $z_\sigma = 0.003$. Note that we have obtained the entire redshift posterior from GRIZLI in Section 3.1 and set a criterion of $(\Delta z)_{\text{posterior}}/(1 + z_{\text{peak}}) < 0.002$ for secure redshift measurements. But here we still set a Gaussian prior centered on z_{peak} with $z_\sigma = 0.003$ for simplicity in SED fitting, following Momcheva et al. (2016). Actually, the minimum, median, and maximum values of $\Delta z/(1 + z)$ for our sample are 1.4×10^{-4} , 2.8×10^{-4} , and 1.5×10^{-3} , respectively.

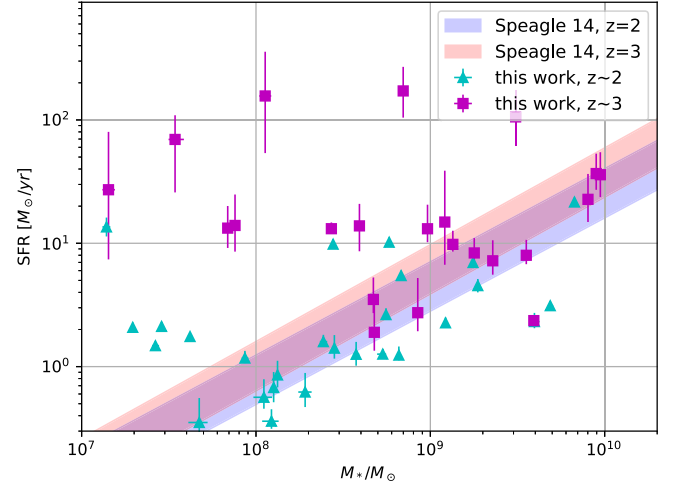


Figure 2. SFR- M_* relation for our galaxy sample, where the low- and high-redshift individual measurements are marked in cyan triangles and magenta squares. As a comparison, we also show the star-forming main sequence fitted by Speagle et al. (2014) with ± 0.2 dex scatters. Sanders et al. (2021) give results fairly close to their extrapolated best fit out to $\log(M_*/M_\odot) = 9$.

Our mass estimates are in agreement with Santini et al. (2023), even though we stress that our results are more robust, because we use spectroscopic redshifts. After correcting magnification according to our recent lensing model (Bergamini et al. 2023a), we are allowed to take a glimpse of the loci of our galaxies in the SFR- M_* diagram as in Figure 2. We show the star-forming main sequence fitted by Speagle et al. (2014), which is extrapolated from $\log(M_*/M_\odot) \in [9.7, 11.1]$ to the mass range of our sample with ± 0.2 dex scatters. Sanders et al. (2021) give stacked results of field galaxies fairly close to their extrapolated best fit out to $\log(M_*/M_\odot) = 9$. Our sample generally scatters around the main sequence at higher M_* . But at lower M_* high-SFR galaxies are dominant, especially for $z \sim 3$ at $M_*/M_\odot \lesssim 3 \times 10^8$. It might account for the low metallicity at the low-mass region when assuming the FMR (Mannucci et al. 2010), which will be discussed in Section 4.1.

3.4. AGN Contamination

The metallicity diagnostics used in this work are strictly for star-forming regions/galaxies, and the results will be incorrect if there is AGN emission. So the last step is to exclude the AGN contamination from purely star-forming galaxies, by using the mass-excitation (MEx) diagram as shown in Figure 3. AGNs leave strong signatures on nebular line ratios such as $\text{O III } \lambda 5007/\text{H}\beta$ and/or $\text{N II } \lambda 6584/\text{H}\alpha$, which form the most traditional version of the BPT diagram (Baldwin et al. 1981). Due to the limited spectral resolution of JWST/NIRISS slitless spectroscopy ($R \sim 150$), $[\text{N II}]$ is entirely blended with $\text{H}\alpha$, which precludes us from using the BPT diagram to remove AGN contamination.

Fortunately, Juneau et al. (2014) proposed an effective approach coined the MEx diagram, using M_* as a proxy for $[\text{N II}]/\text{H}\alpha$, which functions well at $z \sim 0$ (i.e., SDSS DR7). Coil et al. (2015) further modified the MEx demarcation by horizontally shifting these curves to high M_* by 0.75 dex, which is shown to be more applicable to the MOSDEF sample (Sanders et al. 2021) at $z \sim 2.3$. We thus rely on this modified MEx to prune AGN contamination from our galaxy sample. As shown in Figure 3, the green and red curves mark the steep

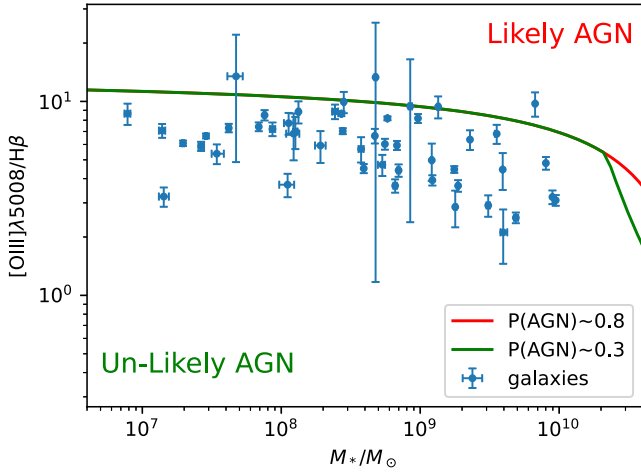


Figure 3. The mass-excitation diagram of our sample, used to exclude possible AGN galaxies. The positions of the likely AGN galaxies with the possibility of 0.8 and 0.3 are marked by the red and green curves. No significant possible AGN contamination is evident in our samples, with one galaxy (ID = 03854) only slightly off by 1σ .

gradient of $P(\text{AGN}) \sim 0.3$ and $P(\text{AGN}) \sim 0.8$, respectively, which represent the probability that the galaxy hosts an AGN.

Most of the sources are clearly unlikely AGN, and some scattered around the critical line are ambiguous. There are only two galaxies slightly above the upper demarcation within 1σ . Because our analysis is based on stacking, a small minority of contaminating AGN will have a negligible impact. Given the limited sample size, we tend to retain more applicable data, and consequently, no possible AGN is eliminated and we preserve all 50 galaxies.

3.5. Stacking Spectra

Robust emission lines are required to estimate metallicity for MZR measurement. So we need composite spectra obtained by stacking procedure to achieve higher S/N from low-resolution grism spectra. In the previous subsection, we have selected 50 spectroscopically confirmed galaxies in the A2744-lensed field that are undergoing active star formation. Then they are divided into two redshift bins ($z \in [1.8, 2.3]$ and $z \in [2.6, 3.4]$), and three mass bins, respectively, as in Table 2. Our choice of binning aims to have a reasonable number of galaxies per bin. We tested that changing the mass bins does not significantly affect our conclusions. Approximately each mass bin contains ~ 7 individual galaxies, and the S/N will be increased roughly by a factor of $\sqrt{7} = 2.6$. The 1D/2D spectra of representative galaxies in each of the six bins are shown in Figure 1.

Then we adopt the following stacking procedures, similar to those utilized by Henry et al. (2021) and Wang et al. (2022b):

1. Subtract continuum models from the extracted grism spectra. The continua are constructed by GRIZLI combining two orients. We apply a multiplicative factor to the continuum models to make sure there is no offset between the modeled and observed continuum levels around emission lines, to avoid continuum oversubtraction.
2. Normalize the continuum-subtracted spectrum of each object using its measured [O III] flux, to avoid excessive weighting toward objects with stronger line fluxes. Here the [O III] fluxes we used are the results of 1D line profile

fitting instead of 2D forward modeling by GRIZLI, for a more straightforward normalization.

3. De-redshift each normalized spectrum to its rest frame, and resample on the same wavelength grid using SPECTRES²⁶ with the integrated flux preservation.
4. Take the median and the variance of the normalized fluxes at each wavelength grid as the value and uncertainty of the stacked spectrum.

As shown in Figure 4, these key lines are more significant in stacked spectra. The (relative) emission line fluxes are measured by fitting a set of Gaussian profiles to the line in stacked spectra, as well as individual spectra. We simultaneously fit [O II], [Ne III], H δ , H γ , H β , [O III], H α , and [S II]. The amplitude ratio of [O III] $\lambda\lambda 4960, 5008$ doublets is fixed to 1:2.98 following Storey & Zeppen (2000). The centroids of Gaussian profiles are allowed a small shift of the corresponding rest-frame wavelengths of emission lines, within $\pm 10 \text{ \AA}$, in order to accommodate systematic uncertainties. The FWHMs of each line are not required to be the same, but are set between $[10, 25] \text{ \AA}$, consistent with the rest-frame spectral resolution $\Delta\lambda \approx 7 \text{ \AA}$ corresponding to $R \approx 150$ for NIRISS. We use the software LMFIT²⁷ to perform the nonlinear least-squares minimization, with the measured quantities summarized in Table 2. The stacked metallicity is estimated using the same methods as the individual galaxies outlined in Section 3.2. Our later discussion will mainly focus on the stacked results.

4. Results

From the joint analysis of the JWST/NIRISS and JWST/NIRCam data, we revisit the measurement of the MZR using the stacked spectra of the A2744-lensed field galaxies within the mass range of $M_* \in (10^{6.9}, 10^{10.0}) M_\odot$ at $z \in (1.8, 3.4)$, shown in Section 4.1. We also perform a systematic investigation of the differences between 2D and 1D forward-modeled fluxes of nebular emission lines from slitless spectroscopy, as detailed in Section 4.2.

4.1. The MZR at the Low-mass End

Our key scientific result is the measurement of the gas-phase MZR in the low mass range of $\log(M_*/M_\odot) \in (6.9, 10.0)$ at $z \in (1.8, 3.4)$. The slope of the MZR has been shown to be a key diagnostic of galaxy chemical evolution and the cycling of baryons and metals through star formation and gas flows (see e.g., Maiolino & Mannucci 2019, and references therein). In particular, Sanders et al. (2021) argue that the shape of the MZR at $z \sim 2-3$ is more tightly regulated by the efficiency of metal removal by gas outflows ζ_{out} , rather than by the change of gas fractions with stellar mass $\mu_{\text{gas}}(M_*)$. Henry et al. (2013a) observe a steepening of the MZR slope at $z \sim 2$, suggesting a transition from momentum-driven winds to energy-driven winds as the primary prescription for galactic outflows in the low-mass end.

We find a clear correlation between metallicity and stellar mass for both individual galaxies and stacked spectra at $z \in [1.8, 2.3]$ and $z \in [2.6, 3.4]$, as shown in the left panel of Figure 5. The $z \sim 2$ and $z \sim 3$ individual galaxy samples have Spearman correlation coefficients of 0.788 and 0.688 with p -values of 6.36×10^{-7} and 3.98×10^{-4} , respectively. We

²⁶ <https://spectres.readthedocs.io/en/latest/>

²⁷ <https://lmfit.github.io/lmfit-py/>

Table 2
Measured Properties of the Stacked Spectra

Group	N_{gal}	Mass Range	$\log M_*^{\text{med}}$	[O III]/H β	[O II]/H β	[O III]/[O II]	H γ /H β	[Ne III]/[O III]	H α /H β	[S II]/H α	12 + log(O/H)
$1.8 < z_{\text{grism}} < 2.3$											
11	7	[6.8,7.7)	7.42	7.21 ± 0.55	0.75 ± 0.07	9.62 ± 0.58	0.26 ± 0.04	0.07 ± 0.01	2.88 ± 0.26	0.01 ± 0.02	$8.00^{+0.05}_{-0.04}$
12	10	[7.7,8.7)	8.20	7.27 ± 0.63	1.40 ± 0.16	5.20 ± 0.44	0.13 ± 0.07	0.01 ± 0.02	2.77 ± 0.29	0.08 ± 0.03	$8.15^{+0.05}_{-0.05}$
13	11	[8.7,9.9)	9.09	4.84 ± 0.23	1.93 ± 0.15	2.51 ± 0.17	0.09 ± 0.05	0.02 ± 0.02	3.56 ± 0.24	0.09 ± 0.03	$8.37^{+0.04}_{-0.05}$
$2.6 < z_{\text{grism}} < 3.4$											
21	5	[7.1,8.2)	7.84	5.10 ± 0.64	0.32 ± 0.07	15.83 ± 2.94	...	0.04 ± 0.01	$7.98^{+0.19}_{-0.12}$
22	9	[8.2,9.2)	8.84	7.48 ± 0.55	1.75 ± 0.15	4.29 ± 0.23	0.23 ± 0.15	0.03 ± 0.01	$8.25^{+0.05}_{-0.06}$
23	8	[9.2,10.0)	9.57	3.91 ± 0.33	1.80 ± 0.24	2.17 ± 0.22	0.28 ± 0.16	0.05 ± 0.04	$8.47^{+0.05}_{-0.06}$

Notes.

The multiple emission line flux ratios are measured from the stacked spectra shown in Figure 4. The mass range and the median stellar mass $\log M_*^{\text{med}}$ are both logarithmic values $\log(M_*/M_\odot)$. The metallicity inference is derived from the measured line flux ratios in the stacked spectra presented in each corresponding row, using the method described in Section 3.2. Here we use the strong line calibrations prescribed by Bian et al. (2018, B18) and some others. See Table 1 for the relevant coefficients.

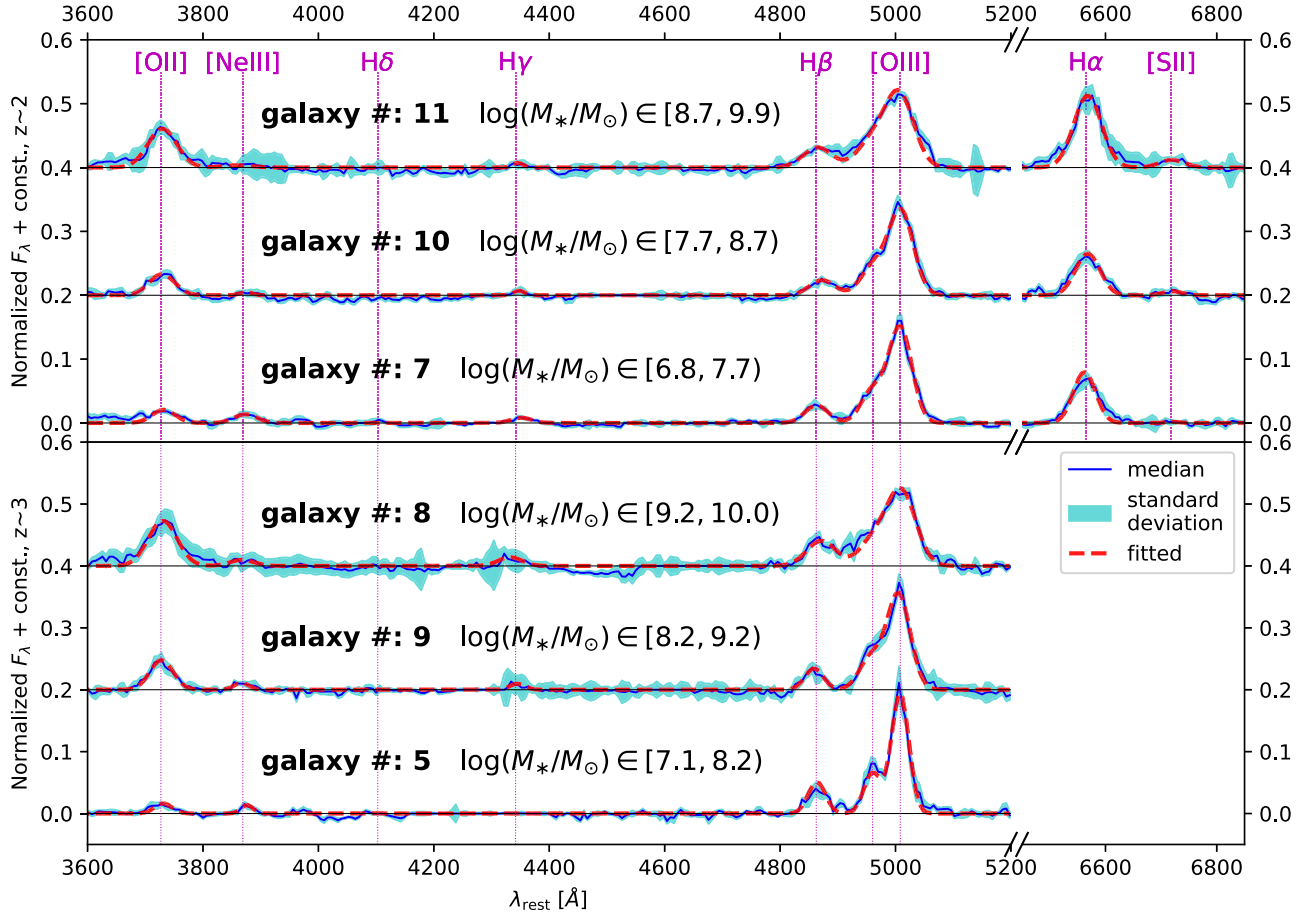


Figure 4. Stacked grism spectra for galaxies residing in several mass bins at two redshift ranges, as shown in the upper ($1.8 < z < 2.3$) and lower ($2.6 < z < 3.4$) panels, respectively. Each mass bin contains 5 ~ 11 galaxies, with the exact number of galaxies and corresponding mass range highlighted above each stacked spectrum. In each set of spectra, the blue curves represent the median stacked spectrum, the cyan bands mark the standard deviation flux uncertainties, and the red dashed curves show the best-fit Gaussian fits to multiple emission lines, while [S II] and H α are across a discontinuous range among other lines (i.e., the [O III] $\lambda\lambda$ 4960,5008 doublets, H β , H γ , H δ , [Ne III], and [O II]) in the broken axes at the right parts. The details of the stacking procedures are presented in Section 3.5.

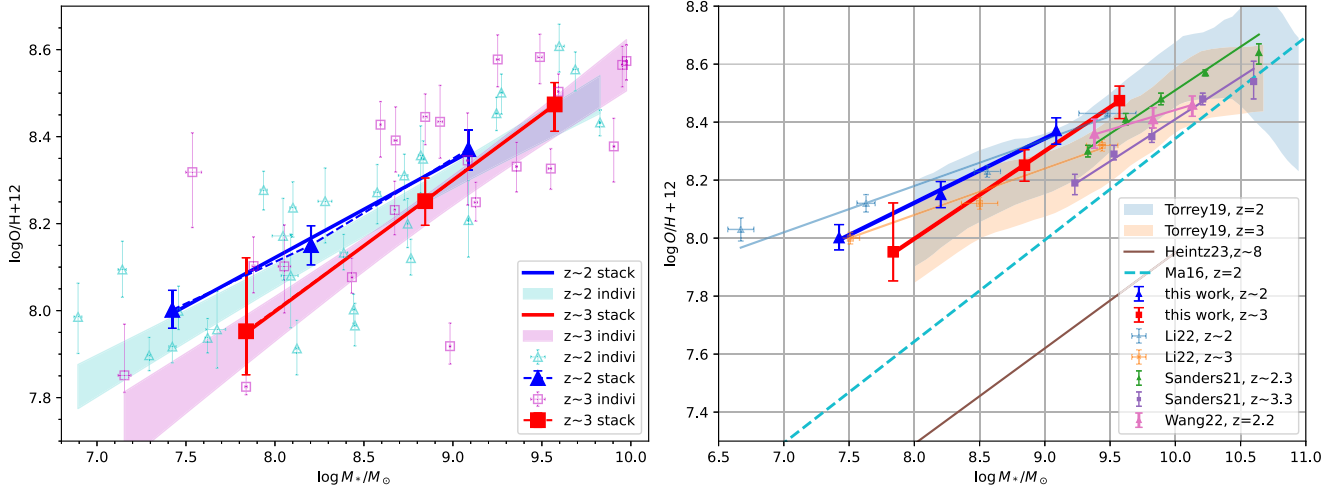


Figure 5. MZR measurements for the star-forming field galaxies behind the A2744 cluster. Left: the individual (hollow) and the stacked (solid) result of our galaxy sample at $z \in [1.8, 2.3]$ (blue triangles) and $z \in [2.6, 3.4]$ (red squares), with their linear fits represented by shaded regions and solid lines. Right: comparison to other observational works, along with the IllustrisTNG100 simulation (Torrey et al. 2019) and the FIRE simulation (Ma et al. 2016). These colored lines are linear regressions of their respective results, with their parameters summarized in Table 3.

perform linear regression over the stacks to derive the MZR:

$$12 + \log(\text{O}/\text{H}) = \beta \times \log(M_*/10^8 M_\odot) + Z_8, \quad (3)$$

where β is the slope and Z_8 is the normalization at $M_* = 10^8 M_\odot$, as the blue and red solid lines with uncertainties at $z \sim 2$ and 3 in both panels of Figure 5. We measure the MZR

Table 3
Comparison of MZR from Different Works, which Is Defined as $12 + \log(\text{O}/\text{H}) = \beta \times \log(M_*/10^8 M_\odot) + Z_8$

Papers	z_{median}	Slope β	Intercept Z_8	Calibration
This work, stack	1.90	0.223 ± 0.017	8.123 ± 0.012	Bian et al. (2018, hereafter B18)
	2.88	0.294 ± 0.010	8.008 ± 0.013	
Individual	1.90	0.229 ± 0.028	8.079 ± 0.027	
	2.88	0.295 ± 0.043	7.981 ± 0.051	
This work, stack	1.90	0.314 ± 0.053	8.064 ± 0.043	Sanders et al. (2023)
	2.88	0.586 ± 0.051	7.748 ± 0.059	
Li et al. (2023)	2	0.16 ± 0.02	8.18 ± 0.03	B18 only O ₃₂
	3	0.16 ± 0.01	8.08 ± 0.01	
Sanders et al. (2021)	2.2	0.30 ± 0.02	7.91 ± 0.04	B18
	3.3	0.29 ± 0.02	7.83 ± 0.04	
Henry et al. (2021)	1.9	0.22 ± 0.03	$7.98 \pm 0.06^*$	Curti et al. (2017)
Wang et al. (2022b)	2.2	0.14 ± 0.02	8.17 ± 0.03	B18
Heintz et al. (2023)	7–10	0.33	7.29	Sanders et al. (2023)
Curti et al. (2023b)	3–6	0.21 ± 0.04	7.80 ± 0.03	Laseter et al. (2023)
Nakajima et al. (2023)	4–10	0.25 ± 0.03	$7.74 \pm 0.06^*$	Nakajima et al. (2022)

Note. The intercept provided in Sanders et al. (2021) and Nakajima et al. (2023) is Z_{10} instead of Z_8 , where $Z_8 = -2\beta + Z_{10}$. The errors they correspond to (marked by an asterisk) are only conservative upper limits: $\sigma_8 = \sqrt{(-2)^2\sigma_\beta^2 + \sigma_{Z_{10}}^2 + 2\sigma_{\beta Z_{10}}}$, since we do not know the (negative) covariance $\sigma_{\beta Z_{10}}$ therein.

slope to be $\beta = 0.223 \pm 0.017$ and $\beta = 0.294 \pm 0.010$ for our galaxy samples at $z_{\text{median}} = 1.90$ and $z_{\text{median}} = 2.88$, respectively. We see moderate evolution in the MZR normalization from $z \sim 2$ to $z \sim 3$: $\Delta Z_8 = -0.11 \pm 0.02$. The stacked MZRs demonstrate good agreement with the individual results (linear fits are shown in the shaded regions in the left panel of Figure 5). The large uncertainty of the stacked metallicity in the $z \sim 3$ lowest-mass bin, comes from the limited number of galaxies. More importantly, all five galaxies within this bin are high-SFR galaxies (Figure 2), which might explain their low stacked metallicity, under the assumption that the star-forming main sequence (Speagle et al. 2014) and the FMR (Mannucci et al. 2010) are valid below $M_* \lesssim 8$. A detailed study and characterization of incompleteness at the low-mass end is beyond the scope of this paper and is left for future work.

We summarize our measurements in Table 3, along with other literature results. The right panel of Figure 5 shows the comparisons to other observations and two cosmological hydrodynamic simulations. In addition to $z \sim 2$ and 3, we also include the three latest MZR measurements at a very high redshift from JWST/NIRSpec for comparison. We measure the slope of the MZR to be $\beta \sim 0.25$ for both $z \sim 2$ and $z \sim 3$. Our slopes at low mass are slightly lower than those found by Sanders et al. (2021), but ours are in lower mass ranges. The shallower normalization could be accounted for the MZR evolution from ours $z_{\text{median}} = 1.90$ and 2.88 to theirs $z \sim 2.3$ and 3.3. Furthermore, we follow their analytical model to understand what physical processes set the slope at the dwarf mass range. In the Peeples & Shankar (2011) model, the metallicity of the ISM is expressed as

$$Z_{\text{ISM}} = \frac{y}{\zeta_{\text{out}} - \zeta_{\text{in}} + \alpha\mu_{\text{gas}} + 1}. \quad (4)$$

Following the assumption by Sanders et al. (2021) that the gas fraction $\mu_{\text{gas}} = 10^{\mu_0} M_*^{-0.36}$ ($\mu_0 = 3.89$ and 3.96 for $z \sim 2$ and

3, respectively), the coefficient $\alpha = 0.7 \cdot (0.64 + \beta)$, the nucleosynthetic stellar yield $y/Z_{\text{ISM}} = 10^{9.2 - (12 + \log(\text{O}/\text{H}))}$, and the metal loading factors of inflowing gas accretion $\zeta_{\text{in}} = 0$, we calculate the loading factors of outflowing galactic winds ζ_{out} at each stacked point and linear fit. We get

$$\begin{aligned} z \sim 2: \log(\zeta_{\text{out}}) &= (-0.130 \pm 0.072)m_{10} + (0.408 \pm 0.119), \\ z \sim 3: \log(\zeta_{\text{out}}) &= (-0.332 \pm 0.037)m_{10} + (0.202 \pm 0.035), \end{aligned}$$

where, $m_{10} = \log(M_*/10^{10} M_\odot)$. (5)

And we find that $\log(\zeta_{\text{out}}/\alpha\mu_{\text{gas}})$ is only a little bit above zero over the mass range, with $\zeta_{\text{out}} \approx 1.01 - 1.5 \times \alpha\mu_{\text{gas}}$. Thus, our results indicate that the shallower MZR may be attributed to a shallower M_* scaling of the metal loading of the galactic outflows ζ_{out} at the low-mass end. We generalize their conclusions that outflows ζ_{out} remain the dominant mechanism other than gas fraction μ_{gas} that sets the MZR slope, and μ_{gas} gradually carries more relative importance and rise to nearly the same order as ζ_{out} for the low-mass regime.

Our MZR slope $\beta \sim 0.25$ is steeper than those reported in Li et al. (2023) at the same redshifts and similar mass range as in Table 3. Although we use the same NIRISS data of the A2744-lensed field, we only match 28 out of 50 galaxies with the on-sky distances (d2d) lower than $1''$ to the Abell catalog of Li et al. (2023), and only 18/50 of them are in agreement with our metallicity measurements within 1σ confidence interval. This difference likely arises from the updated calibration files used in our NIRISS data reduction, and from our Bayesian approach in the metallicity inference using multiple line ratios to joint fit other than only [O III]/[O II] from Bian et al. (2018). In addition, we include the new JWST/NIRCam imaging data covering the rest-frame optical wavelength ranges for our sample galaxies (Paris et al. 2023), use more complex SFH (DPL), and employ the latest JWST-based lensing model

(Bergamini et al. 2023a) for more reliable stellar mass estimates. Another source of difference is their choice of exponentially declining SFH (τ model), which may not be appropriate for our high-redshift star-forming galaxies (Reddy et al. 2012), and might introduce a significant bias in stellar mass M_* estimation (Pacifi et al. 2015; Carnall et al. 2018, 2019).

In agreement with previous work, we also find a tendency for the slope of the MZR to flatten out in the low mass at around $M_*/M_\odot \lesssim 10^9$, although not as significant. As for higher redshift $z \sim 3-10$, our inferred slopes β are consistent with those by Curti et al. (2023b) and Nakajima et al. (2023), but our intercept Z_8 are ~ 0.3 dex higher. At that time, the metal might be enriching and hence the MZR might be building up (Curti et al. 2023b), and it is not until the SFR peaks at Cosmic Noon $z \sim 2-3$ that the MZR exhibits a higher intercept.

The MZR measurements are also sensitive to different strong line calibrations, especially for the intercept Z_8 (Kewley & Ellison 2008), as discussed in Section 3.2. In Table 3, we also provide the MZR from stacks using the Sanders et al. (2023) calibration for comparison. Although the measured slopes are significantly steeper than our default B18 MZR, they are still consistent with Heintz et al. (2023) for dwarf galaxies at higher redshift. We fit the stacked result presented by Henry et al. (2021) in the similar mass range, which assumes Curti et al. (2017) calibration. Our slope agrees with theirs $\beta = 0.22 \pm 0.03$, but the intercept is ~ 0.1 dex higher. This agrees with Wang et al. (2022b) and Li et al. (2023), who test that the calibrations of Bian et al. (2018) yielded a steeper MZR than the calibrations of Curti et al. (2017) when analyzing the same data.

Moreover, we compare our results with two simulation works presented separately in Figure 5. Our individual measurements are largely compatible with the result of the simulations ILLUSTRISTNG (Torrey et al. 2019). But several high-metallicity galaxies lift the stacked MZR up high slightly, yielding a steeper slope than they predicted. Our measured slopes are in better agreement with the FIRE simulation results (Ma et al. 2016), which are capable of resolving high- z dwarf galaxies with sufficient spatial resolution.

In addition, all the MZRs discussed above are derived from galaxy populations residing in random fields. There has been continuous discussion about the environmental dependence of MZR shapes at high redshifts (Peng & Maiolino 2014; Bahé et al. 2017; Calabrò et al. 2022; Wang et al. 2023). Here we raise one recent observation of the MZR at $z \sim 2.2$ showing a much shallower slope ($\beta = 0.14 \pm 0.02$), measured using the HST grism spectroscopy of 36 galaxies residing in the core of the massive BOSS1244 protocluster (Wang et al. 2022b). Our work presented here confirms the significant difference between the MZR slopes measured in field and overdense environments, indicating the change in metal removal efficiency as a function of the environment.

4.2. Investigation of the Morphological Broadening Effect on Measurements of Line Flux and Metallicity

Since metallicity estimates heavily rely on line flux measurements, in this section we verify that different methodologies in deriving emission line fluxes from the NIRISS slitless spectroscopy with limited spectral resolution do not result in significant biases on the metallicity derivations.

For grism spectroscopy, it has long been recognized that the morphological broadening effect can change the overall

spectral shape and flux levels of galaxies (see, e.g., van Dokkum et al. 2011; Wang et al. 2019, 2020). We thus systematically compare, for the first time, two methods to measure emission line flux from slitless spectroscopy, with and without the consideration of this morphological broadening effect. The 2D forward-modeling analysis of GRIZLI is depicted in Section 3.1. In this section, we describe the line profile fitting to 1D extracted spectra using LMFIT. The morphology of a galaxy has already been taken into account when forward modeling its 2D spectrum by GRIZLI. The extracted 1D spectra are morphologically broadened along the dispersion direction, and can vary significantly in spectral slope and flux level for the same object due to the different projected 1D morphology (see Figures 8 and 9 of Wang et al. 2019 for examples). Therefore, we regard the 2D line flux as the reference intrinsic value and 1D flux as the measurement not corrected for the morphology. The difference has not yet been fully investigated, and thus demands immediate attention, with the upcoming advent of large slitless spectroscopic surveys, e.g., Euclid, Roman, and the Chinese Space Station Telescope (CSST).

In the top three panels of Figure 6, we show the comparison between line flux measured from 2D or 1D spectra and try to associate it with the half-light radius r_{50} . The flux ratio of 2D to 1D deviates from 1 tangibly, and 2D flux modeled by GRIZLI are larger in most cases (47/48, 41/48, and 43/48 for [O III], [O II], and H β , respectively) than 1D flux fitted using LMFIT by a median factor of $\sim 30\%$ (with wide dispersion $-0.3-5$, where minus factor means 2D flux is lower than 1D flux). This strong offset does not seem to be related to S/N. As expected, we find it does correlate with the half-light radius r_{50} of the individual galaxies, although not as strong as the Pearson correlation coefficients R shown. The unit of r_{50} is the pixel, and here 1 pixel corresponds to $0''.03$, as illustrated in Section 2. Furthermore, Pearson R decreases as the S/N decreases from the first three brightest lines [O III], [O II] to H β , convincing us of this weak correlation. Linear fitting is employed in an attempt to describe this phenomenon, although it is based on limited data. This nonzero inconsistency first appears when we use 1D [O III] flux to normalize our individual spectra for stacking. We rechecked our MZR using 2D [O III] flux to normalize for stacking, and found the bias of metallicity is lower than 1σ . It indicates that the bias of the two flux measurements may be obscured by the stacking procedure, although we need a larger sample and more tests to verify this assertion. A more significant effect may be seen in the physical quantities directly determined by the line flux value, such as SFR.

Since the flux ratio of 2D to 1D exhibits a correlation with the half-light radius r_{50} , we interpret this discrepancy as a morphological broadening effect. The morphological broadening of the spectrum is not due to physical factors such as velocity dispersion or radiative damping, but is simply an observational effect of the extended source (van Dokkum et al. 2011; Wang et al. 2020). For an ideal point source with no physical broadening effect, the emission line will be measured as a δ function. But if we could spatially resolve the galaxy, which is common in slitless spectroscopy, the emission line would be broadened as a result of the superposition of δ functions from individual pixels. Therefore, more parts of the line edge will be drowned in the noise, resulting in lower total line flux modeled by the Gaussian function. And of course, larger sources produce more broadening, yielding lower flux measurements. We, therefore, deem the top three panels of

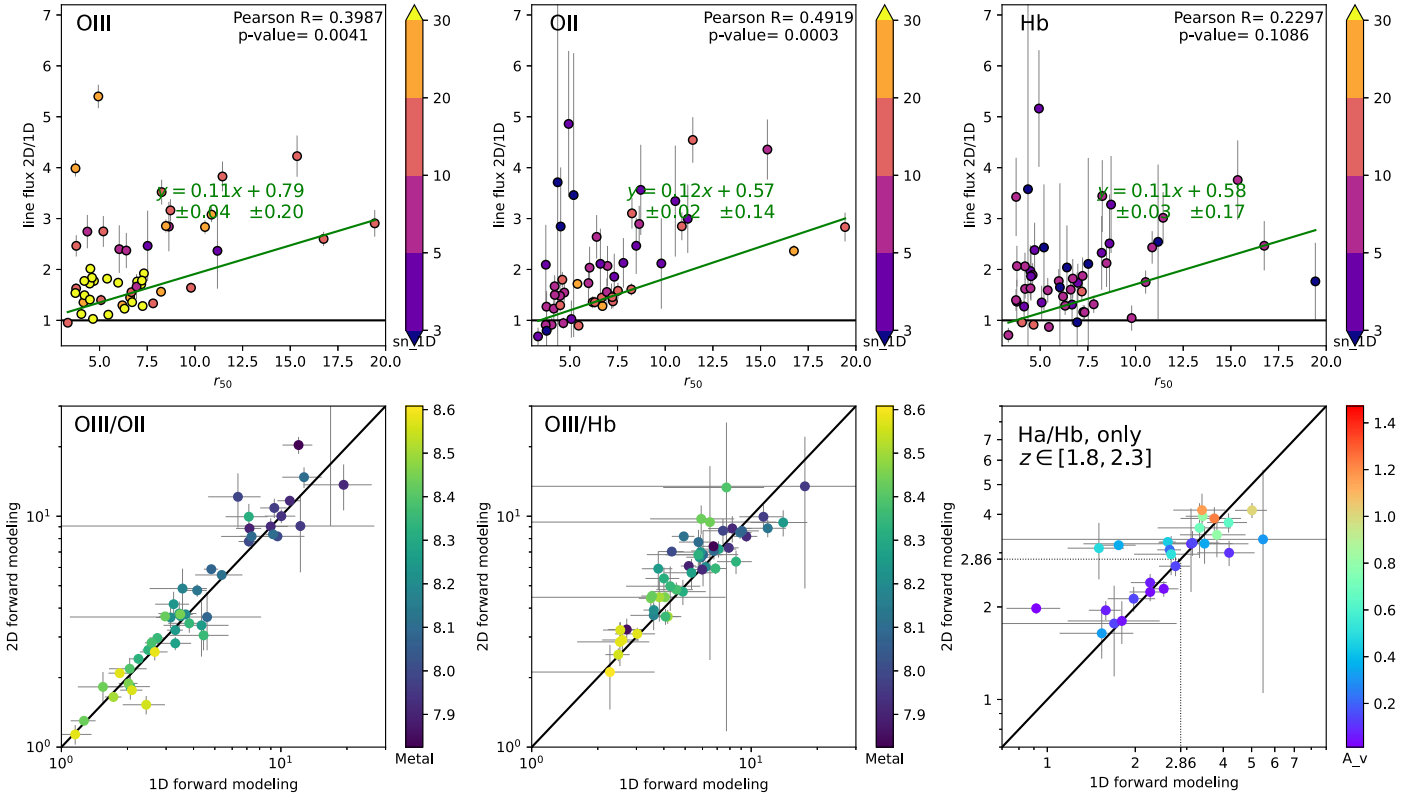


Figure 6. Comparison between the emission line fluxes derived using the 2D/1D forward-modeling methods, explained in detail in Sections 3.1 and 3.5, respectively. The top three panels show the galaxy radius vs. the flux ratio of 2D to 1D for each line. The 2D fluxes are tangibly higher than 1D fluxes (above the black line), and it seems systematic for all three brightest lines of each source (with the same r_{50}). We find a correlation between them (green line), although not so strong, with the Pearson correlation coefficients and the p -value exhibited in the top right corner, as well as the green result of linear fitting at the center. Their color marks the S/N of the flux from the 1D method, showing no significant correlation. The bottom three panels show the line flux ratio, while their color marks the metallicity or the dust extinction derived in Section 3.2 using the GRIZLI flux ratio. These two distributions nearly scatter across the equality line (in black) within the uncertainty. But there are several outliers and a slight systematic overestimation for 2D, which is more obvious for H α /H β at the bottom right.

Figure 6 to be the first attempt to quantitatively analyze the impact of the morphological broadening effect. For large sources ($r_{50} > 10$), the intrinsic flux could be several times larger than the broadened flux.

Although the 2D measurements are larger than the 1D results, in general, it seems that this bias is the same for all emission lines of the same source. As one can notice in the top three panels of Figure 6, for a given source with the same abscissa r_{50} , the corresponding ordinate values 2D/1D of all three lines are quite close to each other, although our naked eye can only recognize those outliers. And we have tested that these patterns are also independent of their S/Ns. Moreover, we show the line flux ratio in the bottom three panels of Figure 6, and they nearly follow the one-on-one line, with few outliers. That means even if this effect is not taken into account like in the 1D method, the flux ratios do not deviate from the 2D method significantly. Therefore, it indicates that the bias of the morphological broadening effect is systematic. We color-code them with the metallicity or the dust extinction A_v derived in Section 3.2 using 2D GRIZLI flux ratio. The color patterns demonstrate the physical meaning of these line ratios, i.e., the gas-phase metallicity diagnostics $O_{32} := [\text{O III}]/[\text{O II}]$, $O_3 := [\text{O III}]/\text{H}\beta$, and the dust extinction indicator $\text{H}\alpha/\text{H}\beta$. The dotted line in the lower right marks the “intrinsic” line ratio in the absence of dust attenuation $\text{H}\alpha/\text{H}\beta = 2.86$. The few sources below it may be due to low S/N and measurement errors (see, e.g., Nelson et al. 2016).

As a consequence, our key result of the metallicity measurement derived from the ratio of two lines in Section 3.2 will not be greatly influenced by the 2D/1D flux measurement method. However the direct line flux (e.g., H β) and the derived quantity (e.g., SFR) of a single emission line could be biased, and for a large source, the intrinsic flux could be several times larger than the measured one. The coarse linear fitting here might describe the distinction between 2D/1D forward-modeling flux of emission line to some extent. We interpret this discrepancy as a morphological broadening effect. We recommend carefully checking the way flux is measured to match the scientific requirement and carefully forward modeling the spectrum through the convolution of the morphological broadening effect. The systematic offset, for the first time, may present an important guideline for future work deriving line fluxes with wide-field slitless spectroscopy, especially for large sky surveys to be conducted by, e.g., Euclid, Roman, and CSST, where it is time-consuming for 2D emission line modeling.

5. Conclusions

We have presented a comprehensive measurement of the MZR at a dwarf mass range using grism slitless spectroscopy. The grism data are acquired by the GLASS-JWST ERS program, targeting the A2744-lensed field. From the joint analysis of the JWST/NIRISS and JWST/NIRCam data, we select a secure sample of 50 field galaxies with $M_*/M_\odot \in [10^{6.9}, 10^{10.0}]$ and $12 + \log(\text{O}/\text{H}) \in [7.8, 8.7]$ at two redshift

ranges $z \in [1.8, 2.3]$ and $z \in [2.6, 3.4]$, assuming the strong line calibration of Bian et al. (2018). Our galaxies are divided into several mass bins and their spectra are stacked to increase the S/N. Then we apply our forward-modeling Bayesian metallicity inference method to the stacked line fluxes. We derive the MZR in the A2744 lensed field as $12 + \log(\text{O}/\text{H}) = \beta \times \log(M_*/10^8 M_\odot) + Z_8$ with $\beta = 0.223 \pm 0.017$ and $\beta = 0.294 \pm 0.010$ in these two redshift ranges $z_{\text{median}} = 1.90$ and $z_{\text{median}} = 2.88$, respectively, as well as a slight evolution: $\Delta Z_8 = -0.11 \pm 0.02$, as presented in Table 3 and Figure 5. Our MZRs have slopes that are consistent with those reported by Sanders et al. (2021) at the higher-mass end and similar redshifts, suggesting that gas outflow mechanisms with the same metal removal efficiency extend to the low-mass regime ($\lesssim 10^9 M_*$) at Cosmic Noon. This M_* scaling of metallicity is well reproduced by the FIRE simulations (Ma et al. 2016).

In addition, we assess the impact of the morphological broadening on emission line measurement by comparing two methods of using 2D forward modeling and line profile fitting to 1D extracted spectra. We show that ignoring the morphological broadening effect when deriving line fluxes from grism spectra results in a systematic reduction of flux by $\sim 30\%$ on average. The coarse linear fitting in Figure 6 could characterize the impact of the morphological broadening effect on modeling the emission line flux to some extent. The direct value (e.g., $\text{H}\beta$) and derived quantity (e.g., SFR) of a single emission line flux could be biased, if one does not account for the galaxy morphology. However, this systematic effect does not significantly influence the line ratio and its derived quantities, e.g., metallicity, dust extinction, age, etc. For this reason, we recommend careful inspection of the line modeling, especially for the next generation of large sky surveys, e.g., Euclid, Roman, and CSST.

Acknowledgments

We would like to thank the anonymous referee for the constructive comments that help us improve the clarity of this Letter. This Letter is dedicated to the memory of our beloved colleague Mario Nonino who passed away prematurely. We miss him and are indebted to him for his countless contributions to the GLASS-JWST project. This work is based on observations made with the NASA/ESA/CSA James Webb Space Telescope. The data were obtained from the Mikulski Archive for Space Telescopes at the Space Telescope Science

Institute, which is operated by the Association of Universities for Research in Astronomy, Inc., under NASA contract NAS 5-03127 for JWST. These observations are associated with program JWST-ERS-1324. We acknowledge financial support from NASA through grant JWST-ERS-1324. X.H. thanks Xiaolei Meng, Lei Sun, and Lilan Yang for the useful discussion. We thank the entire GLASS team that helped shape the manuscript. X.W. is supported by the Fundamental Research Funds for the Central Universities, and the CAS Project for Young Scientists in Basic Research, grant No. YSBR-062. This research is supported in part by the Australian Research Council Centre of Excellence for All Sky Astrophysics in 3 Dimensions (ASTRO 3D), through project number CE170100013. We acknowledge support from the INAF Large grant 2022 ‘‘Extragalactic Surveys with JWST’’ (PI Pentericci). B.M. is supported by an Australian Government Research Training Program (RTP) Scholarship. K.G. is supported by the Australian Research Council through the Discovery Early Career Researcher Award (DECRA) Fellowship (project number DE220100766) funded by the Australian Government.

Facilities: JWST (NIRISS, NIRCame), HST (ACS, WFC3).

Software: GRIZLI (Brammer & Matharu 2021), BAGPIPES (Carnall et al. 2018), LMFIT (Newville et al. 2021), EMCEE (Foreman-Mackey et al. 2013).

Appendix A Measured Quantities of Our Sample

In Table A1, we show the observed and measured physical properties of all 50 galaxies in our sample, including galaxy ID (ID Grism), coordinates (R.A. and Decl.) and grism redshift (z_{grism}) analyzed by GRIZLI, the matched ID in photometry of Paris et al. (2023) (ID Photo.), the stellar mass M_* estimated by SED fitting, the gravitational lensing magnification μ calculated using the model of Bergamini et al. (2023a), and the dust attenuation (A_ν), the dereddened Balmer emission line flux $f_{\text{H}\beta}$ (with its derived SFR), and the gas-phase metallicity $12 + \log(\text{O}/\text{H})$ jointly estimated using our Bayesian method. Note that M_* and SFR have already been corrected by lensing magnification μ , but $f_{\text{H}\beta}$ has not. In Table A2, we exhibit the emission line flux measurements by the 2D/1D method, which are discussed in detail in Section 4.2. Note that all f_{line} are not corrected by μ .

Table A1
Measured Properties of Individual Galaxies

ID Grism	R.A. (deg)	Decl. (deg)	z_{grism}	ID Photo.	$\log(M_*/M_\odot)$	μ	A_V	Dereddened $f_{\text{H}\beta}$ ($10^{-17} \text{ erg s}^{-1} \text{ cm}^{-2}$)	SFR ($M_\odot \cdot \text{yr}^{-1}$)	12+ log(O/H)
(1)	(2)	(3)	(4)	(5)	(6)	(7)	(8)	(9)	(10)	(11)
$1.8 < z_{\text{grism}} < 2.3$										
00765	3.5863967	-30.4093408	2.014	04016	$7.458^{+0.008}_{-0.008}$	4.97	$0.45^{+0.10}_{-0.10}$	$2.69^{+0.24}_{-0.22}$	$2.12^{+0.19}_{-0.17}$	$8.00^{+0.06}_{-0.04}$
00902	3.6170966	-30.4083725	1.876	04154	$8.089^{+0.041}_{-0.053}$	1.68	$0.14^{+0.24}_{-0.11}$	$0.18^{+0.05}_{-0.02}$	$0.36^{+0.09}_{-0.05}$	$8.08^{+0.10}_{-0.12}$
01331	3.5766842	-30.4060897	1.808	04499	$8.101^{+0.016}_{-0.017}$	2.37	$0.70^{+0.30}_{-0.28}$	$0.53^{+0.18}_{-0.13}$	$0.68^{+0.23}_{-0.16}$	$8.24^{+0.06}_{-0.07}$
01365	3.6141973	-30.4060640	2.275	04375	$9.597^{+0.029}_{-0.020}$	1.77	$0.10^{+0.17}_{-0.07}$	$0.78^{+0.14}_{-0.09}$	$2.32^{+0.41}_{-0.27}$	$8.61^{+0.05}_{-0.06}$
02128	3.5985318	-30.4017605	2.009	05117	$7.293^{+0.009}_{-0.008}$	3.55	$0.21^{+0.11}_{-0.10}$	$1.90^{+0.18}_{-0.15}$	$2.08^{+0.20}_{-0.17}$	$7.90^{+0.04}_{-0.04}$
02332	3.6023553	-30.4007355	1.804	05120	$8.727^{+0.020}_{-0.032}$	2.55	$0.05^{+0.09}_{-0.04}$	$1.08^{+0.11}_{-0.08}$	$1.26^{+0.13}_{-0.05}$	$8.31^{+0.05}_{-0.06}$
02696	3.6164407	-30.3977732	1.996	05681	$8.386^{+0.022}_{-0.020}$	1.65	$0.11^{+0.14}_{-0.08}$	$0.69^{+0.09}_{-0.05}$	$1.59^{+0.22}_{-0.11}$	$8.13^{+0.04}_{-0.04}$
02793	3.6041872	-30.3971816	2.068	05706	$9.272^{+0.006}_{-0.007}$	2.10	$0.65^{+0.15}_{-0.15}$	$2.29^{+0.30}_{-0.27}$	$4.53^{+0.60}_{-0.54}$	$8.50^{+0.04}_{-0.05}$
03393	3.6060398	-30.3935272	2.177	06411	$8.450^{+0.007}_{-0.006}$	1.93	$0.34^{+0.26}_{-0.21}$	$0.58^{+0.16}_{-0.10}$	$1.41^{+0.39}_{-0.25}$	$7.97^{+0.05}_{-0.05}$
03557	3.6118150	-30.3924863	2.278	06511	$8.442^{+0.006}_{-0.008}$	1.75	$0.01^{+0.02}_{-0.01}$	$3.26^{+0.08}_{-0.07}$	$9.84^{+0.23}_{-0.20}$	$8.00^{+0.04}_{-0.03}$
03666	3.6042544	-30.3916573	1.880	06722	$8.574^{+0.018}_{-0.018}$	1.91	$0.80^{+0.27}_{-0.14}$	$0.73^{+0.19}_{-0.24}$	$1.26^{+0.33}_{-0.07}$	$8.27^{+0.06}_{-0.07}$
03784	3.6031401	-30.3910461	2.177	06860	$7.622^{+0.013}_{-0.014}$	1.99	$0.04^{+0.07}_{-0.03}$	$0.74^{+0.05}_{-0.03}$	$1.75^{+0.11}_{-0.06}$	$7.94^{+0.04}_{-0.03}$
03785	3.6132702	-30.3910937	1.879	06796	$8.832^{+0.008}_{-0.008}$	1.67	$1.02^{+0.11}_{-0.11}$	$2.77^{+0.27}_{-0.25}$	$5.47^{+0.54}_{-0.49}$	$8.35^{+0.04}_{-0.05}$
03854	3.5867377	-30.3907657	2.206	06519	$9.827^{+0.003}_{-0.004}$	6.37	$1.47^{+0.09}_{-0.09}$	$28.19^{+2.24}_{-2.07}$	$21.60^{+1.72}_{-1.59}$	$8.43^{+0.03}_{-0.03}$
04001	3.6100121	-30.3894795	2.173	07049	$8.746^{+0.002}_{-0.002}$	1.73	$0.14^{+0.14}_{-0.10}$	$0.97^{+0.12}_{-0.08}$	$2.64^{+0.33}_{-0.22}$	$8.20^{+0.06}_{-0.05}$
04457	3.5869454	-30.3870037	1.858	07544	$7.936^{+0.020}_{-0.018}$	3.60	$0.14^{+0.15}_{-0.12}$	$1.32^{+0.19}_{-0.11}$	$1.17^{+0.17}_{-0.10}$	$8.28^{+0.04}_{-0.05}$
04482	3.5819407	-30.3866370	1.884	07610	$8.282^{+0.037}_{-0.039}$	3.69	$0.49^{+0.40}_{-0.30}$	$0.69^{+0.30}_{-0.17}$	$0.62^{+0.27}_{-0.15}$	$8.25^{+0.08}_{-0.10}$
04539	3.5988518	-30.3863743	1.857	07644	$8.819^{+0.012}_{-0.012}$	2.09	$0.15^{+0.19}_{-0.10}$	$0.81^{+0.14}_{-0.08}$	$1.24^{+0.22}_{-0.12}$	$8.36^{+0.07}_{-0.09}$
04579	3.5993864	-30.3861434	2.060	07704	$8.045^{+0.047}_{-0.060}$	2.07	$0.32^{+0.15}_{-0.22}$	$0.28^{+0.23}_{-0.05}$	$0.56^{+0.11}_{-0.11}$	$8.17^{+0.09}_{-0.10}$
04611	3.5790397	-30.3859412	2.187	07751	$7.423^{+0.021}_{-0.019}$	3.65	$0.04^{+0.07}_{-0.03}$	$1.13^{+0.07}_{-0.05}$	$1.48^{+0.09}_{-0.06}$	$7.92^{+0.04}_{-0.04}$
04842	3.5992144	-30.3841762	2.028	08183	$7.675^{+0.048}_{-0.063}$	2.00	$0.31^{+0.47}_{-0.04}$	$0.18^{+0.10}_{-0.08}$	$0.35^{+0.20}_{-0.09}$	$7.96^{+0.09}_{-0.09}$
04946	3.5701934	-30.3837325	1.860	08099	$9.245^{+0.004}_{-0.004}$	2.96	$0.81^{+0.10}_{-0.09}$	$6.44^{+0.55}_{-0.50}$	$6.98^{+0.59}_{-0.54}$	$8.45^{+0.04}_{-0.04}$
05123	3.5920216	-30.3825005	1.860	08565	$6.894^{+0.021}_{-0.022}$	2.52	$1.16^{+0.27}_{-0.27}$	$3.38^{+0.85}_{-0.68}$	$4.31^{+1.08}_{-0.86}$	$7.99^{+0.08}_{-0.08}$
05715	3.6103731	-30.3801845	1.877	08541	$9.688^{+0.017}_{-0.013}$	1.75	$0.07^{+0.10}_{-0.05}$	$1.66^{+0.26}_{-0.08}$	$3.12^{+0.04}_{-0.15}$	$8.55^{+0.04}_{-0.05}$
05747	3.5985949	-30.3785188	1.915	09272	$9.087^{+0.003}_{-0.003}$	1.97	$0.07^{+0.12}_{-0.06}$	$1.29^{+0.14}_{-0.07}$	$2.26^{+0.24}_{-0.13}$	$8.21^{+0.09}_{-0.09}$
05770	3.5997721	-30.3778656	1.880	09586	$8.124^{+0.008}_{-0.007}$	1.94	$0.52^{+0.29}_{-0.10}$	$0.50^{+0.15}_{-0.18}$	$0.86^{+0.26}_{-0.18}$	$7.91^{+0.06}_{-0.06}$
05866	3.5911011	-30.3816997	1.883	08556	$8.764^{+0.002}_{-0.002}$	2.53	$0.36^{+0.07}_{-0.07}$	$7.80^{+0.48}_{-0.44}$	$10.20^{+0.63}_{-0.58}$	$8.12^{+0.04}_{-0.04}$
05952	3.5950311	-30.3761179	1.832	09990	$7.142^{+0.022}_{-0.023}$	2.06	$1.23^{+0.21}_{-0.21}$	$9.04^{+1.73}_{-1.48}$	$13.57^{+2.59}_{-2.22}$	$8.09^{+0.06}_{-0.06}$
$2.6 < z_{\text{grism}} < 3.4$										
00073	3.5893372	-30.4159113	2.647	02987	$9.594^{+0.002}_{-0.002}$	3.02	$0.04^{+0.07}_{-0.03}$	$0.94^{+0.09}_{-0.07}$	$2.36^{+0.24}_{-0.18}$	$8.50^{+0.04}_{-0.04}$
00671	3.5845970	-30.4097995	2.657	03939	$8.673^{+0.003}_{-0.003}$	3.94	$0.30^{+0.35}_{-0.22}$	$1.80^{+0.91}_{-0.41}$	$3.50^{+1.78}_{-0.79}$	$8.23^{+0.07}_{-0.06}$
01192	3.6134541	-30.4068477	2.848	04407	$7.536^{+0.051}_{-0.037}$	1.87	$3.46^{+0.38}_{-0.82}$	$14.35^{+8.19}_{-43.64}$	$69.48^{+39.67}_{-43.64}$	$8.32^{+0.09}_{-0.13}$
01514	3.6074237	-30.4064785	3.196	04281	$9.358^{+0.002}_{-0.002}$	2.47	$0.31^{+0.32}_{-0.21}$	$1.49^{+0.70}_{-1.65}$	$7.21^{+3.37}_{-1.65}$	$8.33^{+0.06}_{-0.06}$
01588	3.6129938	-30.4050844	3.043	04550	$8.844^{+0.010}_{-0.011}$	1.87	$1.95^{+0.38}_{-0.43}$	$30.17^{+17.12}_{-11.84}$	$171.88^{+97.54}_{-67.45}$	$8.45^{+0.05}_{-0.06}$
01589	3.6128172	-30.4049834	3.042	04444	$9.489^{+0.012}_{-0.013}$	1.88	$1.60^{+0.41}_{-0.45}$	$18.68^{+11.97}_{-7.79}$	$105.86^{+67.84}_{-44.17}$	$8.58^{+0.05}_{-0.06}$
01659	3.6198203	-30.4043177	2.922	04709	$8.984^{+0.003}_{-0.003}$	1.72	$0.34^{+0.23}_{-0.24}$	$2.34^{+1.33}_{-0.52}$	$13.11^{+7.44}_{-2.91}$	$7.92^{+0.05}_{-0.04}$
02025	3.5982393	-30.4023120	2.651	04978	$8.593^{+0.002}_{-0.002}$	4.30	$1.50^{+0.36}_{-0.41}$	$7.80^{+3.96}_{-2.95}$	$13.84^{+7.03}_{-5.22}$	$8.43^{+0.05}_{-0.07}$
02389	3.6094671	-30.4003762	2.665	05237	$9.550^{+0.003}_{-0.013}$	1.94	$0.18^{+0.24}_{-0.31}$	$2.01^{+0.67}_{-0.12}$	$7.99^{+2.68}_{-1.22}$	$8.33^{+0.05}_{-0.05}$
02621	3.6136448	-30.3986436	2.843	05484	$9.252^{+0.008}_{-0.007}$	1.80	$0.16^{+0.22}_{-0.12}$	$1.67^{+0.53}_{-0.30}$	$8.35^{+2.67}_{-1.50}$	$8.58^{+0.06}_{-0.06}$
02654	3.6118526	-30.3981734	3.041	05594	$8.928^{+0.013}_{-0.012}$	1.89	$0.33^{+0.51}_{-0.25}$	$0.49^{+0.44}_{-0.14}$	$2.74^{+2.49}_{-0.80}$	$8.43^{+0.08}_{-0.08}$
02703	3.6093784	-30.3983894	2.691	05425	$9.975^{+0.002}_{-0.002}$	1.94	$0.79^{+0.37}_{-0.37}$	$8.82^{+4.61}_{-3.01}$	$35.95^{+18.77}_{-12.26}$	$8.57^{+0.04}_{-0.04}$
02855	3.5749452	-30.3967746	3.125	05793	$8.053^{+0.035}_{-0.034}$	3.71	$2.84^{+0.73}_{-0.95}$	$51.19^{+65.75}_{-33.57}$	$156.43^{+200.91}_{-102.59}$	$8.10^{+0.10}_{-0.11}$
02913	3.6078376	-30.3962862	2.666	05857	$8.679^{+0.008}_{-0.009}$	2.12	$0.36^{+0.50}_{-0.26}$	$0.52^{+0.49}_{-0.15}$	$1.90^{+1.78}_{-0.55}$	$8.39^{+0.08}_{-0.07}$
03018	3.6070933	-30.3956151	2.980	06039	$7.838^{+0.006}_{-0.006}$	2.10	$0.79^{+0.38}_{-0.33}$	$2.75^{+1.41}_{-0.85}$	$13.27^{+6.78}_{-4.10}$	$7.82^{+0.03}_{-0.02}$
03531	3.6112440	-30.3924593	2.981	06626	$7.154^{+0.037}_{-0.035}$	1.81	$2.65^{+0.94}_{-1.13}$	$4.85^{+9.43}_{-3.53}$	$27.17^{+52.86}_{-19.77}$	$7.85^{+0.12}_{-0.04}$
04898	3.6022598	-30.3843036	2.663	07846	$9.904^{+0.004}_{-0.003}$	1.96	$0.59^{+0.40}_{-0.35}$	$5.77^{+3.50}_{-1.99}$	$22.71^{+13.78}_{-7.84}$	$8.38^{+0.06}_{-0.08}$
05184	3.5859437	-30.3821176	3.053	08570	$7.880^{+0.007}_{-0.008}$	3.28	$1.19^{+0.51}_{-0.44}$	$4.26^{+3.33}_{-1.65}$	$13.95^{+10.91}_{-5.39}$	$8.10^{+0.07}_{-0.06}$
05343	3.5778395	-30.3811884	3.390	08654	$9.129^{+0.008}_{-0.011}$	3.45	$0.14^{+0.22}_{-0.31}$	$2.45^{+0.71}_{-1.23}$	$9.80^{+2.84}_{-1.23}$	$8.25^{+0.05}_{-0.04}$
05475	3.6060732	-30.3801651	2.691	08838	$9.951^{+0.003}_{-0.003}$	1.82	$0.42^{+0.32}_{-0.26}$	$8.46^{+1.41}_{-2.21}$	$36.75^{+16.57}_{-9.62}$	$8.56^{+0.04}_{-0.05}$
05526	3.5914083	-30.3797763	2.718	08958	$8.432^{+0.004}_{-0.003}$	2.53	$0.07^{+0.11}_{-0.05}$	$4.10^{+0.51}_{-0.24}$	$13.12^{+1.63}_{-0.78}$	$8.08^{+0.04}_{-0.04}$
06057	3.6033100	-30.3742575	3.043	10305	$9.083^{+0.006}_{-0.006}$	1.84	$0.94^{+0.73}_{-0.63}$	$2.58^{+4.15}_{-1.42}$	$14.86^{+23.91}_{-8.17}$	$8.35^{+0.11}_{-0.10}$

Note. Column (1) is the source ID reduced from JWST/NIRISS Grism data by our source detection GRIZLI procedure. Columns (2) and (3) are the equatorial coordinates R.A. and decl. in equinox with an epoch of J2000. Column (4) is the secure redshift determined by GRIZLI in Section 3.1. Column (5) is the matched ID of the GLASS photometric catalog Paris et al. (2023). Column (6) is the stellar mass fitted from the catalog. Column (7) is the magnification of the gravitational lensing effect by the A2744 cluster. Columns (8) and (9) are the dust attenuation A_V and dereddened $\text{H}\beta$ flux estimated in Section 3.2. Column (10) is the star formation rate determined by dereddened $f_{\text{H}\beta}$. Column (11) is gas-phase metallicity represented by oxygen abundance.

Table A2
Flux Derived from 2D/1D Forward Modeling of the Individual Galaxies

ID	R.A. (deg)	Dec. (deg)	z_{grism}	2D Forward Modeling of Emission Line Fluxes f_{line} [$10^{-17}\text{erg s}^{-1}\text{cm}^{-2}$]							1D Extracted Line Profile Fitting of Emission Line Fluxes f_{line} [$10^{-17}\text{erg s}^{-1}\text{cm}^{-2}$]						
				[O II]	[Ne III]	H γ	H β	[O III]	H α	[S II]	[O II]	[Ne III]	H γ	H β	[O III]	H α	[S II]
(1)	(2)	(3)	(4)	(5)	(6)	(7)	(8)	(9)	(10)	(11)	(12)	(13)	(14)	(15)	(16)	(17)	(18)
1.8 < z_{grism} < 2.6																	
00765	3.5863967	-30.4093408	2.014	1.44 ± 0.07	0.69 ± 0.09	...	1.69 ± 0.05	14.92 ± 0.10	5.49 ± 0.09	0.77 ± 0.08	1.52 ± 0.15	1.04 ± 0.11	...	1.84 ± 0.10	14.51 ± 0.19	4.77 ± 0.16	0.79 ± 0.16
00902	3.6170966	-30.4083725	1.876	0.37 ± 0.10	0.11 ± 0.12	0.17 ± 0.07	0.20 ± 0.05	1.82 ± 0.09	0.35 ± 0.07	0.11 ± 0.07	0.11 ± 0.08	0.01 ± 0.06	...	0.08 ± 0.04	0.66 ± 0.07	0.14 ± 0.06	0.02 ± 0.05
01331	3.5766842	-30.4060897	1.808	0.42 ± 0.05	0.07 ± 0.06	0.10 ± 0.03	0.25 ± 0.05	2.31 ± 0.08	0.89 ± 0.07	0.21 ± 0.08	0.33 ± 0.06	0.07 ± 0.04	...	0.18 ± 0.05	1.42 ± 0.07	0.60 ± 0.07	0.19 ± 0.08
01365	3.6141973	-30.4060640	2.275	2.00 ± 0.20	0.86 ± 0.42	0.02 ± 0.35	0.61 ± 0.17	1.72 ± 0.23	1.96 ± 0.22	0.77 ± 0.23	0.67 ± 0.13	0.24 ± 0.13	0.73 ± 0.21	0.74 ± 0.16	0.42 ± 0.18
02128	3.5985318	-30.4017605	2.009	1.04 ± 0.06	0.71 ± 0.08	...	1.52 ± 0.05	12.32 ± 0.09	4.65 ± 0.08	0.19 ± 0.07	1.14 ± 0.15	0.84 ± 0.16	...	1.58 ± 0.12	10.95 ± 0.21	4.15 ± 0.22	0.17 ± 0.17
02332	3.6023553	-30.4007355	1.804	3.37 ± 0.40	1.28 ± 1.12	...	1.31 ± 0.16	8.22 ± 0.23	2.35 ± 0.24	...	0.95 ± 0.21	0.40 ± 0.11	2.60 ± 0.16	0.72 ± 0.16	...
02696	3.6164407	-30.3977732	1.996	1.10 ± 0.07	0.21 ± 0.08	...	0.59 ± 0.05	6.98 ± 0.09	1.77 ± 0.07	0.08 ± 0.08	0.71 ± 0.07	0.14 ± 0.06	...	0.25 ± 0.05	3.93 ± 0.09	1.04 ± 0.08	0.04 ± 0.05
02793	3.6041872	-30.3971816	2.068	2.41 ± 0.10	0.15 ± 0.22	0.03 ± 0.27	1.08 ± 0.07	5.30 ± 0.11	4.07 ± 0.12	0.71 ± 0.12	1.77 ± 0.14	...	0.38 ± 0.13	0.74 ± 0.11	4.09 ± 0.17	3.07 ± 0.16	0.37 ± 0.16
03393	3.6060398	-30.3935272	2.177	0.36 ± 0.03	0.23 ± 0.05	0.10 ± 0.06	0.39 ± 0.05	5.21 ± 0.09	1.26 ± 0.08	0.15 ± 0.08	0.24 ± 0.03	0.20 ± 0.04	3.02 ± 0.07	0.69 ± 0.07	0.11 ± 0.06
03557	3.6118150	-30.3924863	2.278	3.72 ± 0.13	1.31 ± 0.20	1.64 ± 0.20	4.33 ± 0.15	40.62 ± 0.28	8.57 ± 0.18	...	1.11 ± 0.36	...	0.54 ± 0.29	2.47 ± 0.31	14.33 ± 0.66	2.27 ± 0.38	...
03666	3.6042544	-30.3916573	1.880	0.50 ± 0.06	0.13 ± 0.07	0.12 ± 0.04	0.33 ± 0.05	2.51 ± 0.07	1.14 ± 0.06	0.14 ± 0.06	0.40 ± 0.08	0.12 ± 0.06	0.14 ± 0.04	0.26 ± 0.06	1.86 ± 0.08	0.99 ± 0.06	0.17 ± 0.07
03784	3.6031401	-30.3910461	2.177	0.62 ± 0.04	0.33 ± 0.05	0.34 ± 0.05	0.85 ± 0.04	8.27 ± 0.08	1.95 ± 0.06	0.04 ± 0.06	0.41 ± 0.06	0.29 ± 0.06	0.31 ± 0.05	0.52 ± 0.06	5.53 ± 0.10	1.31 ± 0.08	0.07 ± 0.05
03785	3.6132702	-30.3910937	1.879	1.80 ± 0.08	0.24 ± 0.13	0.27 ± 0.07	0.90 ± 0.05	7.12 ± 0.08	3.71 ± 0.07	0.57 ± 0.07	1.39 ± 0.11	0.42 ± 0.09	0.21 ± 0.07	0.55 ± 0.07	5.06 ± 0.11	2.77 ± 0.09	0.31 ± 0.10
03854	3.5867377	-30.3907657	2.206	16.62 ± 0.53	...	3.90 ± 0.76	2.22 ± 0.32	28.81 ± 0.43	27.59 ± 0.47	2.21 ± 0.47	5.87 ± 0.56	1.26 ± 0.51	9.92 ± 0.88	12.02 ± 0.75	1.90 ± 0.72
04001	3.6100121	-30.3894795	2.173	1.45 ± 0.06	0.19 ± 0.08	0.42 ± 0.07	0.90 ± 0.06	7.27 ± 0.10	2.45 ± 0.09	0.24 ± 0.08	0.81 ± 0.06	0.21 ± 0.05	0.23 ± 0.05	0.48 ± 0.05	3.95 ± 0.09	1.31 ± 0.08	...
04457	3.5869454	-30.3870037	1.858	2.67 ± 0.17	0.78 ± 0.35	0.42 ± 0.16	1.04 ± 0.08	10.02 ± 0.13	3.37 ± 0.16	0.66 ± 0.12	1.29 ± 0.23	0.65 ± 0.20	0.12 ± 0.11	0.60 ± 0.12	5.68 ± 0.19	1.88 ± 0.23	0.30 ± 0.17
04482	3.5819407	-30.3866370	1.884	0.76 ± 0.20	...	0.23 ± 0.14	0.43 ± 0.08	3.43 ± 0.12	1.35 ± 0.13	...	0.36 ± 0.12	0.13 ± 0.10	...	0.42 ± 0.06	2.09 ± 0.11	0.62 ± 0.10	...
04539	3.5988518	-30.3863743	1.857	1.10 ± 0.15	...	0.35 ± 0.14	0.91 ± 0.07	4.48 ± 0.10	1.94 ± 0.11	0.32 ± 0.10	0.52 ± 0.16	0.57 ± 0.08	3.09 ± 0.13	1.13 ± 0.13	0.20 ± 0.12
04579	3.5993864	-30.3861434	2.060	0.28 ± 0.06	0.20 ± 0.08	0.15 ± 0.15	0.36 ± 0.05	1.79 ± 0.08	0.59 ± 0.07	0.13 ± 0.07	0.27 ± 0.08	0.07 ± 0.04	0.14 ± 0.06	0.27 ± 0.05	1.28 ± 0.09	0.41 ± 0.08	0.16 ± 0.09
04611	3.5790397	-30.3859412	2.187	0.85 ± 0.07	0.66 ± 0.12	0.63 ± 0.09	1.31 ± 0.07	10.26 ± 0.12	2.93 ± 0.12	...	0.49 ± 0.10	0.20 ± 0.10	0.32 ± 0.09	0.74 ± 0.09	5.89 ± 0.16	1.66 ± 0.15	...
04842	3.5992144	-30.3841762	2.028	0.14 ± 0.05	0.07 ± 0.06	...	0.09 ± 0.06	1.67 ± 0.10	0.31 ± 0.08	0.05 ± 0.09	0.04 ± 0.04	0.03 ± 0.05	0.61 ± 0.06	0.14 ± 0.05	...
04946	3.5701934	-30.3837325	1.860	6.04 ± 0.20	1.46 ± 0.32	0.93 ± 0.19	2.56 ± 0.10	15.20 ± 0.16	10.09 ± 0.18	3.20 ± 0.24	4.40 ± 0.41	0.64 ± 0.32	0.50 ± 0.28	2.20 ± 0.24	11.87 ± 0.39	7.47 ± 0.43	1.95 ± 0.57
05123	3.5920216	-30.3825005	1.860	0.70 ± 0.18	0.80 ± 0.23	0.41 ± 0.13	0.98 ± 0.12	11.33 ± 0.20	4.06 ± 0.17	...	0.33 ± 0.09	0.28 ± 0.08	0.13 ± 0.05	0.29 ± 0.05	2.84 ± 0.10	0.97 ± 0.08	0.05 ± 0.05
05715	3.6103731	-30.3801845	1.877	2.99 ± 0.26	0.24 ± 0.52	...	1.82 ± 0.11	6.09 ± 0.15	4.36 ± 0.13	0.30 ± 0.16	1.41 ± 0.30	...	0.17 ± 0.18	1.38 ± 0.16	4.56 ± 0.24	3.10 ± 0.25	0.53 ± 0.24
05747	3.5985949	-30.3785188	1.915	1.82 ± 0.18	...	0.26 ± 0.17	1.69 ± 0.10	8.82 ± 0.15	3.29 ± 0.13	0.24 ± 0.13	1.23 ± 0.17	0.41 ± 0.14	0.20 ± 0.10	1.08 ± 0.10	5.16 ± 0.16	1.71 ± 0.13	0.22 ± 0.13
05770	3.5997721	-30.3778656	1.880	0.20 ± 0.05	0.05 ± 0.04	0.12 ± 0.03	0.32 ± 0.04	3.74 ± 0.07	0.94 ± 0.06	...	0.07 ± 0.02	...	0.03 ± 0.02	0.17 ± 0.04	1.86 ± 0.06	0.45 ± 0.06	...
05866	3.5911011	-30.3816997	1.883	7.90 ± 0.28	1.44 ± 0.52	2.12 ± 0.23	5.38 ± 0.12	58.64 ± 0.23	17.07 ± 0.17	1.58 ± 0.16	4.25 ± 1.03	2.19 ± 0.88	0.51 ± 0.60	4.64 ± 0.53	30.49 ± 0.98	8.14 ± 0.71	1.12 ± 0.66
05952	3.5950311	-30.3761179	1.832	2.28 ± 0.27	0.44 ± 0.36	0.92 ± 0.26	2.63 ± 0.21	24.84 ± 0.40	10.22 ± 0.36	...	0.47 ± 0.13	0.47 ± 0.12	0.18 ± 0.10	0.51 ± 0.11	4.60 ± 0.18	1.90 ± 0.21	...
2.6 < z_{grism} < 3.4																	
00073	3.5893372	-30.4159113	2.647	2.92 ± 0.09	0.68 ± 0.16	0.43 ± 0.14	0.52 ± 0.11	3.07 ± 0.17	1.85 ± 0.18	0.78 ± 0.18	...	0.25 ± 0.24	1.25 ± 0.34
00671	3.5845970	-30.4097995	2.657	2.38 ± 0.07	0.67 ± 0.12	0.53 ± 0.10	1.32 ± 0.11	11.72 ± 0.19	1.38 ± 0.06	0.46 ± 0.06	0.39 ± 0.07	0.83 ± 0.11	6.44 ± 0.17
01192	3.6134541	-30.4068477	2.848	0.21 ± 0.03	0.05 ± 0.03	...	0.39 ± 0.04	2.79 ± 0.08	0.31 ± 0.06	0.12 ± 0.06	...	0.55 ± 0.09	2.93 ± 0.15
01514	3.6074237	-30.4064785	3.196	2.30 ± 0.07	0.17 ± 0.13	0.78 ± 0.16	0.95 ± 0.11	8.07 ± 0.18	1.79 ± 0.09	0.10 ± 0.05	0.60 ± 0.12	0.52 ± 0.09	5.94 ± 0.19
01588	3.6129938	-30.4050844	3.043	4.43 ± 0.18	0.33 ± 0.37	0.93 ± 0.65	3.78 ± 0.27	22.23 ± 0.45	1.56 ± 0.14	0.22 ± 0.11	...	1.55 ± 0.17	7.23 ± 0.31
01589	3.6128172	-30.4049834	3.042	3.91 ± 0.25	0.39 ± 0.42	...	3.47 ± 0.40	13.46 ± 0.66	0.90 ± 0.11	0.26 ± 0.11	...	0.92 ± 0.16	3.18 ± 0.26
01659	3.6198203	-30.4043177	2.922	1.17 ± 0.06	0.79 ± 0.10	56.41 ± 184.72	1.67 ± 0.09	18.21 ± 0.23	0.70 ± 0.08	0.51 ± 0.10	...	0.81 ± 0.10	10.26 ± 0.26
02025	3.5982393	-30.4023120	2.651	1.95 ± 0.05	0.46 ± 0.09	0.56 ± 0.08	1.59 ± 0.08	9.59 ± 0.14	2.18 ± 0.11	0.93 ± 0.11	0.40 ± 0.13	1.83 ± 0.18	8.63 ± 0.28
02389	3.6094671	-30.4003762	2.665	4.12 ± 0.10	0.46 ± 0.22	0.53 ± 0.16	1.46 ± 0.16	13.24 ± 0.24	2.85 ± 0.18	0.82 ± 0.19	...	1.11 ± 0.32	8.52 ± 0.47
02621	3.6136448	-30.3986436	2.843	3.12 ± 0.18	0.78 ± 0.49	0.21 ± 0.54	1.24 ± 0.25	4.72 ± 0.36	1.08 ± 0.12	0.31 ± 0.12	...	0.49 ± 0.16	1.66 ± 0.25
02654	3.6118526	-30.3981734	3.041	0.82 ± 0.11	0.21 ± 0.12	...	0.16 ± 0.12	1.99 ± 0.19	0.40 ± 0.06	0.17 ± 0.07	...	0.10 ± 0.09	0.83 ± 0.14
02703	3.6093784	-30.3983894	2.691	5.58 ± 0.19	0.80 ± 0.28	1.81 ± 0.25	3.77 ± 0.22	15.56 ± 0.43	1.80 ± 0.16	0.09 ± 0.12	0.35 ± 0.13	1.10 ± 0.22	4.42 ± 0.28
02855	3.5749452	-30.3967746	3.125	1.39 ± 0.14	0.44 ± 0.19	0.26 ± 0.56	2.65 ± 0.34	27.32 ± 0.60	0.56 ± 0.11	...	0.48 ± 0.31	1.25 ± 0.22	9.57 ± 0.37
02913	3.6078376	-30.3962862	2.666	0.81 ± 0.07	0.23 ± 0.12	0.08 ± 0.11	0.13 ± 0.12	2.37 ± 0.17	0.52 ± 0.08	0.1					

ORCID iDs

Xianlong He  <https://orcid.org/0000-0002-1336-5100>
 Xin Wang  <https://orcid.org/0000-0002-9373-3865>
 Tucker Jones  <https://orcid.org/0000-0001-5860-3419>
 Tommaso Treu  <https://orcid.org/0000-0002-8460-0390>
 K. Glazebrook  <https://orcid.org/0000-0002-3254-9044>
 Matthew A. Malkan  <https://orcid.org/0000-0001-6919-1237>
 Benedetta Vulcani  <https://orcid.org/0000-0003-0980-1499>
 Benjamin Metha  <https://orcid.org/0000-0002-8632-6049>
 Maruša Bradač  <https://orcid.org/0000-0001-5984-0395>
 Gabriel Brammer  <https://orcid.org/0000-0003-2680-005X>
 Guido Roberts-Borsani  <https://orcid.org/0000-0002-4140-1367>
 Victoria Strait  <https://orcid.org/0000-0002-6338-7295>
 Andrea Bonchi  <https://orcid.org/0000-0002-2667-5482>
 Marco Castellano  <https://orcid.org/0000-0001-9875-8263>
 Adriano Fontana  <https://orcid.org/0000-0003-3820-2823>
 Charlotte Mason  <https://orcid.org/0000-0002-3407-1785>
 Emiliano Merlin  <https://orcid.org/0000-0001-6870-8900>
 Takahiro Morishita  <https://orcid.org/0000-0002-8512-1404>
 Diego Paris  <https://orcid.org/0000-0002-7409-8114>
 Paola Santini  <https://orcid.org/0000-0002-9334-8705>
 Michele Trenti  <https://orcid.org/0000-0001-9391-305X>
 Kristan Boyett  <https://orcid.org/0000-0003-4109-304X>
 K. Grasha  <https://orcid.org/0000-0002-3247-5321>

References

- Andrews, B. H., & Martini, P. 2013, *ApJ*, **765**, 140
- Arellano-Córdova, K. Z., Berg, D. A., Chisholm, J., et al. 2022, *ApJL*, **940**, L23
- Bahé, Y. M., Schaye, J., Crain, R. A., et al. 2017, *MNRAS*, **464**, 508
- Baldry, I. K., Glazebrook, K., & Driver, S. P. 2008, *MNRAS*, **388**, 945
- Baldwin, J. A., Phillips, M. M., & Terlevich, R. 1981, *PASP*, **93**, 5
- Bergamini, P., Acebron, A., Grillo, C., et al. 2023a, *ApJ*, **952**, 84
- Bergamini, P., Acebron, A., Grillo, C., et al. 2023b, *A&A*, **670**, A60
- Bian, F.-Y., Kewley, L. J., & Dopita, M. A. 2018, *ApJ*, **859**, 175
- Brammer, G. 2023, grizli, v1.8.2, Zenodo, doi:10.5281/zenodo.7712834
- Brammer, G. B., & Matharu, J. 2021, gbrammer/grizli: Release 2021, v1.3.2, Zenodo, doi:10.5281/zenodo.5012699
- Brammer, G. B., van Dokkum, P. G., & Coppi, P. 2008, *ApJ*, **686**, 1503
- Bruzual, G., & Charlot, S. 2003, *MNRAS*, **344**, 1000
- Calabrò, A., Guaita, L., Pentericci, L., et al. 2022, *A&A*, **664**, A75
- Calzetti, D., Armus, L., Bohlin, R. C., et al. 2000, *ApJ*, **533**, 682
- Carnall, A. C., Leja, J., Johnson, B. D., et al. 2019, *ApJ*, **873**, 44
- Carnall, A. C., McLure, R. J., Dunlop, J. S., & Davé, R. 2018, *MNRAS*, **480**, 4379
- Chabrier, G. 2003, *PASP*, **115**, 763
- Coil, A. L., Aird, J., Reddy, N. A., et al. 2015, *ApJ*, **801**, 35
- Conroy, C., & van Dokkum, P. G. 2012, *ApJ*, **747**, 69
- Curti, M., Cresci, G., Mannucci, F., et al. 2017, *MNRAS*, **465**, 1384
- Curti, M., D'Eugenio, F., Camiani, S., et al. 2023a, *MNRAS*, **518**, 425
- Curti, M., Maiolino, R., Carniani, S., et al. 2023b, arXiv:2304.08516
- Davé, R., Finlator, K., & Oppenheimer, B. D. 2011, *MNRAS*, **416**, 1354
- Davé, R., Finlator, K., & Oppenheimer, B. D. 2012, *MNRAS*, **421**, 98
- Dekel, A., & Mandelker, N. 2014, *MNRAS*, **444**, 2071
- Erb, D. K., Pettini, M., Shapley, A. E., et al. 2010, *ApJ*, **719**, 1168
- Erb, D. K., Shapley, A. E., Pettini, M., et al. 2006, *ApJ*, **644**, 813
- Finlator, K., & Davé, R. 2008, *MNRAS*, **385**, 2181
- Foreman-Mackey, D., Hogg, D. W., Lang, D., & Goodman, J. 2013, *PASP*, **125**, 306
- Franchetto, A., Mingozzi, M., Poggianti, B. M., et al. 2021, *ApJ*, **923**, 28
- Heintz, K. E., Brammer, G. B., Giménez-Arteaga, C., et al. 2023, *NatAs*, **7**, 1517
- Guo, Y., Koo, D. C., Lu, Y., et al. 2016, *ApJ*, **822**, 103
- Henry, A. L., Martin, C. L., Finlator, K., & Dressler, A. 2013a, *ApJ*, **769**, 148
- Henry, A. L., Rafelski, M. A., Sunnquist, B., et al. 2021, *ApJ*, **919**, 143
- Henry, A. L., Scarlata, C., Domínguez, A., et al. 2013b, *ApJL*, **776**, L27
- Jauzac, M., Richard, J., Jullo, E., et al. 2015, *MNRAS*, **452**, 1437
- Johnson, T. L., Sharon, K., Bayliss, M. B., et al. 2014, *ApJ*, **797**, 48
- Jones, T., Martin, C., & Cooper, M. C. 2015a, *ApJ*, **813**, 126
- Jones, T., Wang, X., Schmidt, K. B., et al. 2015b, *ApJ*, **149**, 107
- Juneau, S., Bournaud, F., Charlot, S., et al. 2014, *ApJ*, **788**, 88
- Kennicutt, R. C. J. 1998, *ARA&A*, **36**, 189
- Kewley, L. J., & Ellison, S. L. 2008, *ApJ*, **681**, 1183
- Kewley, L. J., Nicholls, D. C., & Sutherland, R. S. 2019, *ARA&A*, **57**, 511
- Kümmel, M., Walsh, J. R., Pirzkal, N., Kuntschner, H., & Pasquali, A. 2009, *PASP*, **121**, 59
- Langeroodi, D., Hjorth, J., Chen, W., et al. 2023, *ApJ*, **957**, 39
- Laseter, I. H., Maseda, M. V., Curti, M., et al. 2023, arXiv:2306.03120
- Li, M., Cai, Z., Bian, F., et al. 2023, *ApJL*, **955**, L18
- Lilly, S. J., Carollo, C. M., Pipino, A., Renzini, A., & Peng, Y.-j. 2013, *ApJ*, **772**, 119
- Lotz, J. M., Koekemoer, A., Coe, D., et al. 2017, *ApJ*, **837**, 97
- Lu, Y., Blanc, G. A., & Benson, A. J. 2015a, *ApJ*, **808**, 129
- Lu, Y., Mo, H., & Lu, Z. 2015b, arXiv:1504.02109
- Ma, X., Hopkins, P. F., Faucher-Giguère, C.-A., et al. 2016, *MNRAS*, **456**, 2140
- Madau, P., & Dickinson, M. 2014, *ARA&A*, **52**, 415
- Maiolino, R., & Mannucci, F. 2019, *A&ARv*, **27**, 3
- Maiolino, R., Nagao, T., Grazian, A., et al. 2008, *A&A*, **488**, 463
- Mannucci, F., Cresci, G., Maiolino, R., Marconi, A., & Gnerucci, A. 2010, *MNRAS*, **408**, 2115
- Matthee, J., Mackenzie, R., Simcoe, R. A., et al. 2023, *ApJ*, **950**, 67
- Momcheva, I. G., Brammer, G. B., van Dokkum, P. G., et al. 2016, *ApJS*, **225**, 27
- Muzzin, A., Marchesini, D., Stefanon, M., et al. 2013, *ApJS*, **206**, 8
- Nakajima, K., Ouchi, M., Isobe, Y., et al. 2023, *ApJS*, **269**, 33
- Nakajima, K., Ouchi, M., Xu, Y., et al. 2022, *ApJS*, **262**, 3
- Nelson, E. J., van Dokkum, P. G., Momcheva, I. G., et al. 2016, *ApJL*, **817**, L9
- Newville, M., Otten, R., Nelson, A., et al. 2021, Imfit/Imfit-py v1.0.2, Zenodo, doi:10.5281/zenodo.4516651
- Pacifici, C., da Cunha, E., Charlot, S., et al. 2015, *MNRAS*, **447**, 786
- Paris, D., Merlin, E., Fontana, A., et al. 2023, *ApJ*, **952**, 20
- Peebles, M. S., & Shankar, F. 2011, *MNRAS*, **417**, 2962
- Peng, Y.-j., & Maiolino, R. 2014, *MNRAS*, **443**, 3643
- Peng, Y.-j., & Maiolino, R. 2014, *MNRAS*, **438**, 262
- Petri, A. 2016, *A&C*, **17**, 73
- Pharo, J., Guo, Y., Calvo, G. B., et al. 2023, *ApJ*, **959**, 48
- Reddy, N. A., Pettini, M., Steidel, C. C., et al. 2012, *ApJ*, **754**, 25
- Rhoads, J. E., Wold, I. G. B., Harish, S., et al. 2023, *ApJL*, **942**, L14
- Roberts-Borsani, G., Morishita, T., Treu, T., et al. 2022, *ApJL*, **938**, L13
- Sanders, R. L., Shapley, A. E., Jones, T. A., et al. 2021, *ApJ*, **914**, 19
- Sanders, R. L., Shapley, A. E., Kriek, M. T., et al. 2015, *ApJ*, **799**, 138
- Sanders, R. L., Shapley, A. E., Topping, M. W., Reddy, N. A., & Brammer, G. B. 2023, arXiv:2303.08149
- Santini, P., Fontana, A., Castellano, M., et al. 2023, *ApJL*, **942**, L27
- Schaerer, D., Marques-Chaves, R., Baruffet, L., et al. 2022, *A&A*, **665**, L4
- Shapley, A. E., Reddy, N. A., Sanders, R. L., Topping, M. W., & Brammer, G. B. 2023, *ApJL*, **950**, L1
- Speagle, J. S., Steinhardt, C. L., Capak, P. L., & Silverman, J. D. 2014, *ApJS*, **214**, 15
- Storey, P. J., & Zeppen, C. J. 2000, *MNRAS*, **312**, 813
- Torrey, P., Vogelsberger, M., Marinacci, F., et al. 2019, *MNRAS*, **484**, 5587
- Tremonti, C. A., Heckman, T. M., Kauffmann, G., et al. 2004, *ApJ*, **613**, 898
- Treu, T., Roberts-Borsani, G., Bradac, M., et al. 2022, *ApJ*, **935**, 110
- Trump, J. R., Arrabal Haro, P., Simons, R. C., et al. 2023, *ApJ*, **945**, 35
- van Dokkum, P. G., Brammer, G., Fumagalli, M., et al. 2011, *ApJL*, **743**, L15
- Wang, K., Wang, X., & Chen, Y. 2023, *ApJ*, **951**, 66
- Wang, X., Jones, T., Vulcani, B., et al. 2022a, *ApJL*, **938**, L16
- Wang, X., Jones, T. A., Treu, T. L., et al. 2017, *ApJ*, **837**, 89
- Wang, X., Jones, T. A., Treu, T. L., et al. 2019, *ApJ*, **882**, 94
- Wang, X., Jones, T. A., Treu, T. L., et al. 2020, *ApJ*, **900**, 183
- Wang, X., Li, Z., Cai, Z., et al. 2022b, *ApJ*, **926**, 70
- Willott, C. J., Doyon, R., Albert, L., et al. 2022, *PASP*, **134**, 025002
- Zahid, H. J., Bresolin, F., Kewley, L. J., Coil, A. L., & Davé, R. 2012, *ApJ*, **750**, 120
- Zahid, H. J., Kashino, D., Silverman, J. D., et al. 2014, *ApJ*, **792**, 75
- Zahid, H. J., Kewley, L. J., & Bresolin, F. 2011, *ApJ*, **730**, 137